

# CONSTRAINING THE ACCRETION FLOW IN SGR A\* BY GENERAL RELATIVISTIC DYNAMICAL AND POLARIZED RADIATIVE MODELING

ROMAN V. SHCHERBAKOV<sup>1</sup>, ROBERT F. PENNA<sup>2</sup>, JONATHAN C. MCKINNEY<sup>3</sup>

*Draft version October 15, 2019*

## ABSTRACT

Constraints on the Sgr A\* black hole and accretion flow parameters are found by fitting polarized sub-mm observations to three-dimensional (3D) general relativistic (GR) magnetohydrodynamical (MHD) (GRMHD) simulations. We compile a mean Sgr A\* spectrum by averaging observations over many epochs from reports in 29 papers in order to determine the mean flux  $F_\nu$ , linear polarization (LP) fractions, circular polarization (CP) fractions, and electric vector position angles (EVPA). GRMHD simulations are run with dimensionless spins  $a_* = 0, 0.5, 0.7, 0.9, 0.98$  over a  $20000M$  time interval. We perform GR polarized radiative transfer using our new code to explore the spin  $a_*$ , inclination angle  $\theta$ , position angle (PA), accretion rate  $\dot{M}$ , and electron temperature  $T_e$  at radius  $6M$ . We perform  $\chi^2$  per degrees of freedom (dof) statistical analysis for 88 GHz to 857 GHz. Fitting mean fluxes (without LP and CP fractions) across all spins gives a best  $\chi^2/\text{dof} < 1$  and wide confidence intervals, which suggests that polarization may be crucial for constraining spin. Fitting with mean fluxes and LP and CP fractions favors spin  $a_* = 0.5$  with 1) minimum  $\chi^2/\text{dof} \approx 2.09$  and 90% confidence intervals of  $\theta = 60^\circ - 69^\circ$ ,  $\text{PA} = 69^\circ - 109^\circ$ ,  $\dot{M} = (3.8 - 5.0) \times 10^{-8} M_\odot \text{year}^{-1}$ ,  $T_e = (3.4 - 4.2) \cdot 10^{10}$  K at  $6M$ ; 2) CP being produced mainly by Faraday conversion; and 3) an emission region size at 230 GHz that is consistent with VLBI size of  $37\mu\text{as}$ .

*Subject headings:* accretion, accretion disks – black hole physics – Galaxy: center – radiative transfer – relativistic processes — polarization

## 1. INTRODUCTION

The mass of the Galactic Center black hole (BH) is  $M \approx 4.5 \cdot 10^6 M_\odot$  (Ghez et al. 2008; Reid et al. 2008) and the spin is uncertain (Huang et al. 2009b; Broderick et al. 2009; Moscibrodzka et al. 2009; Broderick et al. 2010; Dexter et al. 2010). It resides at a distance  $d \approx 8.4$  kpc. Because of its proximity, it has been observed in many wavelengths:  $\gamma$ -rays, X-rays, IR, (sub-)mm, and radio. X-ray bremsstrahlung emission originates from hot gas near the radius of BH gravitational influence (Narayan, Yi & Mahadevan 1995; Narayan et al. 1998; Shcherbakov & Baganoff 2010) and Compton-scattered emission close to the horizon (Moscibrodzka et al. 2009). X-rays at large radius are spatially resolved and have been used to constrain dynamical models for this region (Shcherbakov & Baganoff 2010). The sub-mm emission is cyclo-synchrotron originating close to the BH. Cyclo-synchrotron emission is polarized and both linear and circular polarizations have been observed from Sgr A\* at several sub-mm wavelengths. The accretion flow was recently resolved at 230 GHz (Doeleman et al. 2008; Fish et al. 2011). General relativistic (GR) effects were deemed necessary to explain the small size with

full width at half maximum (FWHM) of  $37\mu\text{as}$ . Radio emission is also produced by cyclo-synchrotron, but at larger distances from the BH. Relativistic frame-dragging is important near the BH, so sub-mm polarized observations and the Compton-scattered X-rays can provide constraints on the BH spin. The goal of the present paper is to model the sub-mm in the range 88 GHz to 857 GHz in order to estimate the accretion flow parameters including a preliminary estimate of black hole spin.

Sgr A\* is a variable source with a variability amplitude routinely reaching 30% in sub-mm. A popular approach is to fit simultaneous observations (e.g. Yuan, Quataert & Narayan 2004; Broderick et al. 2009), in particular the set from Falcke et al. (1998). However, in such an approach one would use a single simultaneous set of observations. In addition, simultaneous observations of fluxes, linear polarization (LP), and circular polarization (CP) fractions at several frequencies are not available. So we consider non-simultaneous statistics of all observations at all frequencies and find the mean values and standard errors of quantities at each frequency. We check that samples of observed fluxes and LP fractions are consistent with a Gaussian distribution at  $\nu \geq 88$  GHz.

Numerous accretion flow models have been applied to the Galactic Center: advection-dominated accretion flow (ADAF) (Narayan & Yi 1995), advection-dominated inflow-outflow solution (ADIOS) (Blandford & Begelman 1999), jet-ADAF (Yuan, Markoff & Falcke 2002), jet (Maitra, Markoff & Falcke 2009), and viscous and magnetohydrodynamical (MHD) numerical simulations. The quasi-analytical models are useful because there is little expense in changing parameters. However,

roman@astro.umd.edu

<sup>1</sup> <http://astroman.org>

Department of Astronomy, University of Maryland, College Park, MD 20742-2421, USA; Hubble Fellow

<sup>2</sup> rpenna@cfa.harvard.edu

Harvard-Smithsonian Center for Astrophysics, 60 Garden Street, Cambridge, MA 02138, USA

<sup>3</sup> jmckinne@stanford.edu

Department of Physics and Kavli Institute for Particle Astrophysics and Cosmology, Stanford University, Stanford, CA 94305-4060, USA; Chandra Fellow

they have a large number of free parameters and also incorporate many assumptions that are not justifiable from first principles (Huang et al. 2008, 2009a), which leads to systematic uncertainties in any fits. Numerical simulations require fewer inputs and are useful for more quantitative modeling of the plasma near a rotating BH. However, general relativistic (GR) MHD (GRMHD) simulations (especially three-dimensional (3D) simulations) run over a sufficiently long duration are still computationally expensive and involve state-of-the-art codes that are still being developed (McKinney & Blandford 2009; Fragile et al. 2009; Noble & Krolik 2009; Moscibrodzka et al. 2009; Penna et al. 2010). Yet, 3D GRMHD simulations are required to model the flow near a rotating black hole because the flow's behavior is qualitatively different in 2D axisymmetry and 3D (e.g. Igumenshchev 2008) due to generalizations of Cowling's anti-dynamo theorem (Hide & Palmer 1982). Given their expense, such 3D GRMHD simulations are limited to a region relatively close to the BH (Dexter et al. 2009; Moscibrodzka et al. 2009), whereas some emission and some Faraday rotation might happen far from the BH. So we analytically extend the modeled region out to  $20000M$ , perform radiative transfer, and find the best fit to the data. The extension to large radius allows us to define the electron temperature more consistently (Sharma et al. 2007). We find a posteriori (see Appendix A) that the simulated polarized spectra are not overly sensitive to the details of the analytic extensions of density and temperature, but may depend on the extension of the magnetic field.

The radiation close to the BH has been modeled in Newtonian (Yuan, Quataert & Narayan 2004) and quasi-Newtonian approximations (Goldston, Quataert & Igumenshchev 2005; Chan et al. 2009). It has been modeled in GR assuming unpolarized (Fuerst & Wu 2004; Dexter et al. 2009; Dolence et al. 2009) and polarized (Broderick et al. 2009; Shcherbakov & Huang 2011) light. Fitting the total flux spectrum might not be sufficient to constrain the spin, and naturally one expects polarization to provide extra constraints. Spin values from  $a_* = 0$  (Broderick et al. 2009) to  $a_* = 0.9$  (Moscibrodzka et al. 2009) have been estimated. We neglect Comptonization (Moscibrodzka et al. 2009) and radiation from non-thermal electrons (Mahadevan 1998; Özel, Psaltis & Narayan 2000; Yuan, Quataert & Narayan 2004). Emissivities are calculated in the synchrotron approximation (Legg & Westfold 1968; Sazonov 1969; Pacholczyk 1970; Melrose 1971) with an exact thermal electron distribution. Discrepancies with the exact cyclo-synchrotron emissivities (Leung, Gammie & Noble 2011; Shcherbakov & Huang 2011) are negligible. Exact Faraday rotation and conversion expressions are used (Shcherbakov 2008).

We compare simulated spectra to observed ones at many frequencies simultaneously, extending an approach pioneered by Broderick et al. (2009) and Dexter et al. (2009). After checking the observations for Gaussianity, computing their means and standard errors, we employ  $\chi^2$  statistics. We search the space of all parameters: spin  $a_*$ , inclination  $\theta$ , ratio of proton to electron temperatures

$T_p/T_e$  at distance  $6M$  from the center, and accretion rate  $\dot{M}$  to find the minimum  $\chi^2$  models. We find models with  $\chi^2$  relatively close to unity. Then we integrate the  $\chi^2$  probability density function (PDF) over the entire parameter space and compute 90% confidence intervals.

We summarize the observational constraints on the accretion flow in the sub-mm in § 2. Our 3D GRMHD simulations are described in § 3 together with the physically-motivated extension to large radii, and the electron heating prescription. We run simulations for dimensionless spins  $a_* = a/M = 0, 0.5, 0.7, 0.9, 0.98$ . The GR polarized radiative transfer technique is described in § 5. The statistical analysis is presented in § 6. The set of observations we consider consists of the spectral energy distribution (SED) within the 88 GHz to 857 GHz frequency range, linear polarization (LP) fractions at 88 GHz, 230 GHz, and 349 GHz, and circular polarization (CP) fractions at 230 GHz and 349 GHz. In § 7 we discuss our results: the best fit models to the observations, the behavior of  $\chi^2$  near the best fits, the importance of various physical effects in producing the observed CP and LP and electric vector position angle (EVPA), image size estimates, and confidence intervals for the fitted quantities. We show the actual images of total and polarized intensities. Discussion in § 8 compares the results to previous estimates, emphasizes the significance of polarization, notes the sources of error, and outlines prospects for future work. We note that fitting the total flux does not strongly constrain the flow. In Appendix A we perform a number of convergence tests of our GR polarized radiative transfer code and the radial extension of the dynamical model. Throughout the paper we measure distance and time in the units of BH mass  $M$  by setting the speed of light  $c$  and gravitational constant  $G$  to unity.

## 2. OBSERVATIONS

Sgr A\* is known to be a highly variable source, yet quiescent models of Sgr A\* emission are popular and useful. Unlike the drastic variations of X-ray and NIR fluxes (Baganoff et al. 2001; Genzel et al. 2003), sub-mm fluxes do not vary by more than a factor of 2 – 3 (Zhao et al. 2003). We approximate the distribution of observed fluxes at each frequency and polarization type by a Gaussian, find the mean and the standard error, and use a  $\chi^2$  analysis. Previously, the observed flux spectra were compiled by Yuan, Quataert & Narayan (2004); Broderick et al. (2009). However, both papers summarize a limited set of observations and do not perform averaging. Sub-mm flux data reported in Yuan, Quataert & Narayan (2004) consists of a short set of observations by Falcke et al. (1998) and one set of SMA observations by Zhao et al. (2003). Broderick et al. (2009) adds to these the rest of SMA total flux data (Marrone et al. 2006a,b, 2007, 2008). So 6 out of at least 29 papers on sub-mm observations of Sgr A\* were employed. We compute an averaged spectrum based on all 29 papers with sub-mm observations of Sgr A\*.

The reported observations vary in period from several hours (An et al. 2005) to several years (Zhao et al. 2003; Krichbaum et al. 2006). We know that variations of a factor of 2 may happen within several hours (Yusef-Zadeh et al. 2009), whereas variations by more than a factor of several are never observed in the sub-mm.

**Table 1**  
Summary of Sgr A\* radio/sub-mm observations

$\nu$ [GHz]	Telescopes	$F_\nu$ [Jy]	LP [%]	CP [%]	EVPA [ $^\circ$ ]
8.45	VLA	$0.683 \pm 0.032$ (Serabyn et al. 1997; Falcke et al. 1998; Bower et al. 1999a; An et al. 2005)	...	$-0.26 \pm 0.06^b$ (Bower et al. 1999a)	...
14.90	VLBA, VLA	$0.871 \pm 0.012^a$ (Serabyn et al. 1997; Falcke et al. 1998; Bower et al. 2002; Herrnstein et al. 2004; An et al. 2005; Yusef-Zadeh et al. 2009)	...	$-0.62 \pm 0.26^b$ (Bower et al. 2002)	...
22.50	VLBA, VLA	$0.979 \pm 0.016^a$ (Serabyn et al. 1997; Falcke et al. 1998; Bower et al. 1999b; Herrnstein et al. 2004; An et al. 2005; Lu et al. 2008; Yusef-Zadeh et al. 2007, 2009)	$0.20 \pm 0.01^b$ (Bower et al. 1999b; Yusef-Zadeh et al. 2007)	...	...
43	GMVA, VLBA, VLA	$1.135 \pm 0.026^a$ (Falcke et al. 1998; Lo et al. 1998; Bower et al. 1999b; Herrnstein et al. 2004; An et al. 2005; Shen et al. 2005; Krichbaum et al. 2006; Yusef-Zadeh et al. 2007; Lu et al. 2008; Yusef-Zadeh et al. 2009)	$0.55 \pm 0.22^b$ (Bower et al. 1999b; Yusef-Zadeh et al. 2007)	...	...
88	BIMA, MPIFR, VLBA, VLA, Nobeyama, NMA, CARMA	$1.841 \pm 0.080$ (Falcke et al. 1998; Krichbaum et al. 1998; Bower et al. 1999b; Doeleman et al. 2001; Miyazaki et al. 2004; Shen et al. 2005; Krichbaum et al. 2006; Macquart et al. 2006; Lu et al. 2008; Yusef-Zadeh et al. 2009)	$1.42 \pm 0.5^{b,c}$ (Bower et al. 1999b; Macquart et al. 2006)	...	$-4^d$ (Bower et al. 1999b; Shen et al. 2005; Macquart et al. 2006)
102	OVRO, CSO-JCMT, Nobeyama, NMA, IRAM	$1.91 \pm 0.15$ (Serabyn et al. 1997; Falcke et al. 1998; Miyazaki et al. 2004; Mauerhan et al. 2005; Yusef-Zadeh et al. 2009)	...	...	...
145	Nobeyama, NMA, IRAM, JCMT	$2.28 \pm 0.26$ (Falcke et al. 1998; Aitken et al. 2000; Miyazaki et al. 2004; Yusef-Zadeh et al. 2009)	...	...	...
230	IRAM, JCMT, BIMA, SMA, OVRO	$2.64 \pm 0.14$ (Serabyn et al. 1997; Falcke et al. 1998; Aitken et al. 2000; Bower et al. 2003, 2005; Zhao et al. 2003; Krichbaum et al. 2006; Marrone et al. 2006a, 2007, 2008; Doeleman et al. 2008; Yusef-Zadeh et al. 2009)	$7.40 \pm 0.66$ (Bower et al. 2003, 2005; Marrone et al. 2007, 2008)	$-1.2 \pm 0.3^b$ (Munoz et al. (2009, 2011))	$111.5 \pm 5.3$ (Bower et al. 2003, 2005; Marrone et al. 2007, 2008)
349	SMA, CSO, JCMT	$3.18 \pm 0.12$ (Aitken et al. 2000; An et al. 2005; Marrone et al. 2006b, 2007, 2008; Yusef-Zadeh et al. 2009)	$6.50 \pm 0.61$ (Marrone et al. 2006b, 2007)	$-1.5 \pm 0.3^b$ (Munoz et al. (2011))	$146.9 \pm 2.2$ (Marrone et al. 2006b, 2007)
674	CSO, SMA	$3.29 \pm 0.35$ (Marrone et al. 2006a, 2008; Yusef-Zadeh et al. 2009)	...	...	...
857	CSO	$2.87 \pm 0.24$ (Serabyn et al. 1997; Marrone et al. 2008; Yusef-Zadeh et al. 2009)	...	...	...

<sup>a</sup>Flux observations at 14.9, 22.5, 43 GHz are inconsistent with a Gaussian distribution (Herrnstein et al. 2004), while other fluxes, CP and LP fractions are consistent with Gaussian distributions.

<sup>b</sup>The uncertainty of the mean of these quantities is given by instrumental errors.

<sup>c</sup>The mean LP at 3.5 mm is computed based on lower and upper sidebands in Macquart et al. (2006). The error is based on 0.5% systematic error reported therein.

<sup>d</sup>The mean EVPA at 88 GHz is uncertain due to  $\pm 180^\circ$  degeneracy; e.g. the reported EVPA =  $80^\circ$  could as well be interpreted as  $-100^\circ$ .

So fluxes observed more than a day apart are weakly correlated. A question of autocorrelation timescales will be addressed in future work. We consider the following averaging technique to sample the distributions of fluxes. First, we define groups of close frequencies, the frequencies in each group being different by no more than several percent from the mean. There are 11 such groups (see Table 1). We exclude papers reporting single frequencies far from the mean of each group. In particular, the 94 GHz and 95 GHz observations of Li et al. (2008); Falcke et al. (1998) and the 112 GHz observations of Bower et al. (2001) are excluded. A mean frequency is ascribed to represent each group. Then we take all reported observations of each polarization type (total flux, LP and CP fraction, EVPA) for each group and draw the largest sample of fluxes/polarization fractions, taking observations performed more than one day apart. When several fluxes are reported over a period of several hours (Yusef-Zadeh et al. 2009), we normally draw one data point from the very beginning of the ob-

servations. Some of the published observations are unreliable. Often unreliable data is produced by observing in sub-mm with large beam size. Light from Sgr A\* is blended with dust and other sources. In particular, SMT data (Yusef-Zadeh et al. 2009), early CSO measurements (Serabyn et al. 1997), and early JCMT measurements (Aitken et al. 2000) may have such issues, so we exclude these data from the sample. The interferometric observations, especially with VLBI, help to reduce an error of otherwise unreliable observations, e.g. with BIMA array (Bower et al. 2001). However, some inconsistencies still exist for simultaneous observations at the same frequency with different instruments (Yusef-Zadeh et al. 2009).

After the sample of fluxes, polarization fractions, and EVPA angles are found for each frequency group, we compute the mean, the standard error and check using the Kolmogorov-Smirnov test that the data are at least not inconsistent with a Gaussian distribution. The summary of results is presented in Table 1. CP fractions of  $-1.2\%$  at 230 GHz and  $-1.5\%$  at 349 GHz are based

on SMA observations by Munoz et al. (2011) with the reported error  $\pm 0.3\%$  of instrumental nature. The  $p$ -values of the Kolmogorov-Smirnov consistency test are above 0.2 for LP and EVPA in each frequency group, which shows the consistency of sample fluxes/LP fractions with a Gaussian distribution and so our  $\chi^2$  analysis is not invalidated. Also,  $p > 0.05$  holds for fluxes at all frequencies except  $\nu = 14.90$  GHz,  $\nu = 22.50$  GHz,  $\nu = 43$  GHz. Exceptionally large samples of  $> 100$  fluxes are reported in Herrnstein et al. (2004) for those frequencies. The flux distribution at  $\nu \leq 43$  GHz is found to be bimodal and inconsistent with a Gaussian. However,  $p = 0.7$  for the Kolmogorov-Smirnov test at  $\nu = 230$  GHz despite a large sample of 50 fluxes. Thus, the current state of observations do not invalidate Gaussian distributions for  $F_\nu$ , LP, CP, and EVPA at frequencies  $\nu \geq 88$  GHz. This allows us to cautiously proceed with  $\chi^2$  statistical analysis based on computed means and standard errors. Note also, that standard errors in our flux samples are smaller than the error bars of old observations (Falcke et al. 1998; Yuan, Quataert & Narayan 2004; Broderick et al. 2009), but the errors are still larger compared to contemporary single-observation instrumental errors (Marrone et al. 2007). That is, we do not incorporate instrumental error in our estimates of standard error of the mean. The same is true for LP and EVPA at 230 GHz and 349 GHz. However, the instrumental error of LP at 88 GHz is large. We do not incorporate the source size measurements (Doeleman et al. 2008) in calculating  $\chi^2$ , but we check that the best fit model is not inconsistent with those observations. Figure 1 shows a compilation of the mean quantities and their Gaussian standard errors. The data are represented by both error bars and the interpolated shaded area in between. A red dashed curve on the  $F_\nu$  plot represents the analytic approximation  $F_\nu = 0.248\nu^{0.45} \exp(-(\nu/1100)^2)$ , where flux is in Jy and frequency is in GHz.

### 3. THREE-DIMENSIONAL GRMHD SIMULATIONS

Our radiative transfer calculations take the results of simulations of accretion flows onto BHs as input. These simulations are similar to those in Penna et al. (2010). We review the methodology.

#### 3.1. Governing equations

We simulate radiatively inefficient accretion flows (RIAFs) onto rotating BHs using a three-dimensional fully general relativistic code (see §3.3). The BH is described by the Kerr metric. We work with Heaviside-Lorentz units. Our five simulations correspond to different choices of the dimensionless BH spin parameter:  $a_* = 0, 0.5, 0.7, 0.9$ , and  $0.98$ . The self-gravity of the RIAF is ignored.

The RIAF is a magnetized fluid, so we solve the GRMHD equations of motion (Gammie et al. 2003). Mass conservation gives:

$$\nabla_\mu(\rho u^\mu) = 0, \quad (1)$$

where  $\rho$  is the fluid frame rest-mass density,  $u^\mu$  is the contravariant 4-velocity, and  $\nabla_\mu$  is the covariant derivative. Energy-momentum conservation gives

$$\nabla_\mu T_\nu^\mu = 0, \quad (2)$$

where the stress energy tensor  $T_\nu^\mu$  includes both matter and electromagnetic terms,

$$T_\nu^\mu = (\rho + u_g + p_g + b^2)u^\mu u_\nu + (p_g + b^2/2)\delta_\nu^\mu - b^\mu b_\nu, \quad (3)$$

where  $u_g$  is the internal energy density and  $p_g = (\Gamma - 1)u_g$  is the ideal gas pressure with  $\Gamma = 4/3$ . Models with  $\Gamma = 5/3$  show minor differences compared to models with  $\Gamma = 4/3$  (McKinney & Gammie 2004; Mignone & McKinney 2007). The contravariant fluid-frame magnetic 4-field is given by  $b^\mu$  and is related to the lab-frame 3-field via  $b^\mu = B^\nu h_\nu^\mu / u^t$  where  $h_\nu^\mu = u^\mu u_\nu + \delta_\nu^\mu$  is a projection tensor, and  $\delta_\nu^\mu$  is the Kronecker delta function (Gammie et al. 2003). We often employ  $\mathbf{b}$  below, which is the orthonormal magnetic field vector in a comoving locally flat reference frame (Penna et al. 2010). The magnetic energy density ( $u_b$ ) and magnetic pressure ( $p_b$ ) are then given by  $u_b = p_b = b^\mu b_\mu / 2 = b^2 / 2 = \mathbf{b}^2 / 2$ . Note that the angular velocity of the gas is  $\Omega = u^\phi / u^t$ .

Magnetic flux conservation is given by the induction equation

$$\partial_t(\sqrt{-g}B^i) = -\partial_j[\sqrt{-g}(B^i v^j - B^j v^i)], \quad (4)$$

where  $v^i = u^i / u^t$ , and  $g = \text{Det}(g_{\mu\nu})$  is the determinant of the metric. No explicit resistivity or viscosity is included.

In Penna et al. (2010), we studied both RIAFs and geometrically thin radiatively efficient disks. For the later case, a cooling term was added to the energy-momentum equation (2) to describe radiative losses and keep the disk thin. The current set of models are all RIAFs, so no cooling term is needed, energy generated by viscous dissipation is advected along with the flow or transported out due to convection or in a wind.

#### 3.2. Physical models

The initial mass distribution is an isentropic equilibrium torus (Chakrabarti 1985a,b; De Villiers, Hawley & Krolik 2003) with pressure  $p = K_0 \rho^{4/3}$  for  $K_0 = 0.009$ . The torus inner edge is at  $r_{\text{in}} = 20M$  and maximum density and pressure are at  $R_{\text{max}} = 65M$ . We initialize the solution so that  $\rho = 1$  at the pressure maximum. As in Chakrabarti (1985a), the angular velocity distribution of the initial torus is a power law, where for the Chakrabarti (1985a)  $q$ -parameter we choose  $q = 1.65$  (At large radii  $\Omega \sim (r/M)^{-q}$ ). The thickness of the torus at the pressure maximum is then  $|h/r| \sim 0.3$ , where

$$|h/r| \equiv \frac{\int \int \int |\theta - \pi/2| \rho(r, \theta, \phi) dA_{\theta\phi} dt}{\int \int \int \rho(r, \theta, \phi) dA_{\theta\phi} dt}, \quad (5)$$

where  $dA_{\theta\phi} \equiv \sqrt{-g}d\theta d\phi$  is an area element in the  $\theta - \phi$  plane, and the integral over  $dt$  is a time average over the period when the disk is in a steady state (see §3.6). A tenuous atmosphere fills the space outside the torus. It has the same polytropic equation of state as the torus,  $p = K_0 \rho^\Gamma$ , with  $\Gamma = 4/3$ , and an initial rest-mass density of  $\rho = 10^{-6}(r/M)^{-3/2}$ , corresponding to a Bondi-like atmosphere. The torus is threaded with three loops of weak, poloidal magnetic field: the initial gas-to-magnetic pressure ratio is  $\beta = p_{g,\text{max}}/p_{b,\text{max}} = 100$ , where  $p_{\text{max}}$  and  $p_{b,\text{max}}$  are the maximum values of the gas and magnetic pressure in the torus. This approach to normalizing the initial field is used in many other studies (Gammie et al.

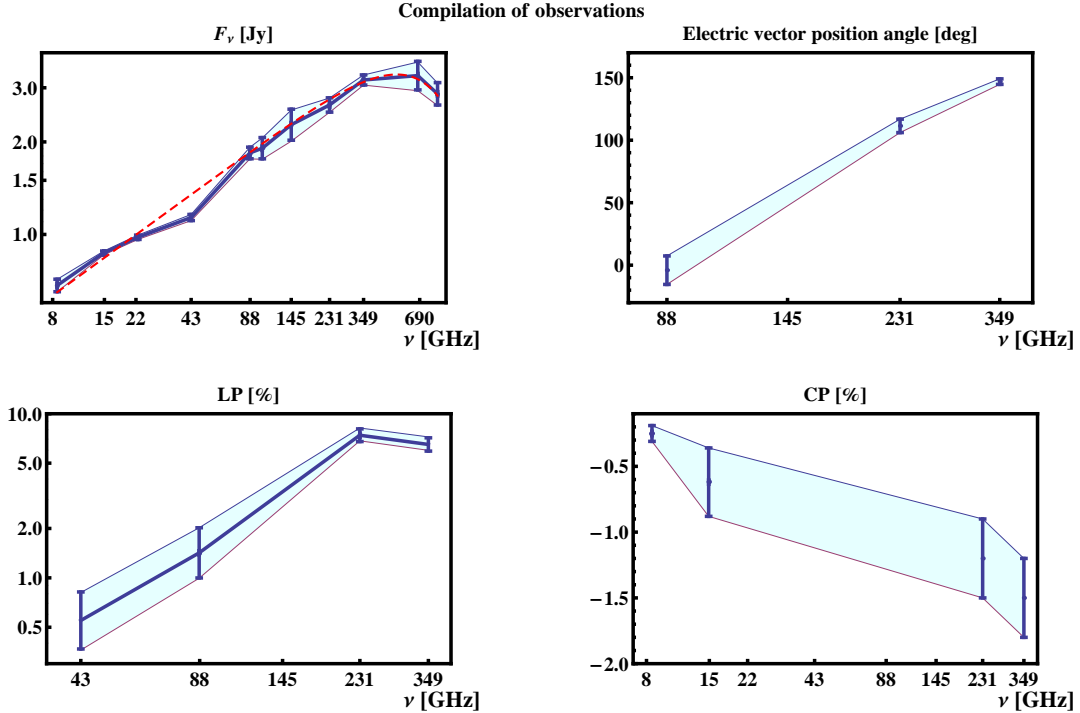


**Figure 1.** Mean observed SEDs of specific flux  $F_\nu$ , linear polarization (LP) fraction, electric vector position angle (EVPA), and circular polarization (CP) fraction. The error bars show  $1\sigma$  standard error of the mean. The dashed line on the  $F_\nu$  plot represents the analytic approximation  $F_\nu(\text{Jy}) = 0.248\nu^{0.45} \exp(-(\nu/1100)^2)$  for frequency  $\nu$  in GHz (not the simulated SED). As noted in Table 1, the error is instrumental for CP at high frequencies and LP at 88 GHz, whereas it is computed from a sample of observed quantities for flux, EVPA at all frequencies, and LP at high frequencies.

2003; McKinney & Gammie 2004; McKinney 2006a; McKinney & Narayan 2007b; Komissarov & McKinney 2007; Penna et al. 2010).

Recent GRMHD simulations of thick disks indicate that the results for the disk (but not the wind-jet, which for us is less important) are roughly independent of the initial field geometry (McKinney & Narayan 2007a,b; Beckwith et al. 2008a). The vector potential we use is the same as in Penna et al. (2010). It is

$$A_{\phi,N} \propto Q^2 \sin\left(\frac{\log(r/S)}{\lambda_{\text{field}}/(2\pi r)}\right) [1 + 0.02(\text{ranc} - 0.5)], \quad (6)$$

with all other  $A_\mu$  initially zero. We use  $Q = (u_g/u_{g,\text{max}} - 0.2)(r/M)^{3/4}$ , and set  $Q = 0$  if either  $r < S$  or  $Q < 0$ . Here  $u_{g,\text{max}}$  is the maximum value of the internal energy density in the torus. We choose  $S = 22M$  and  $\lambda_{\text{field}}/(2\pi r) = 0.28$ , which gives initial poloidal loops that are roughly isotropic such that they have roughly 1:1 aspect ratio in the poloidal plane. The form of the potential in equation (6) ensures that each additional field loop bundle has opposite polarity. Perturbations are introduced to excite the magneto-rotational instability (MRI). The second term on the right-hand-side (RHS) of equation 6 is a random perturbation: ranc is a random real number generator for the domain 0 to 1. Random perturbations were introduced in the initial internal energy density in the same way, with an amplitude of 10%. In Penna et al. (2010), it was found that similar simulations with perturbations of 2% and 10% became turbulent at about the same time, the magnetic field energy at that time was negligibly different, and there was no evidence for significant differences in any quantities

during inflow equilibrium.

### 3.3. Numerical methods

We perform simulations using a fully 3D version of HARM that uses a conservative shock-capturing Godunov scheme (Gammie et al. 2003; Shafee et al. 2008; McKinney 2006b; Noble et al. 2006; Mignone & McKinney 2007; Tchekhovskoy, McKinney & Narayan 2007; McKinney & Blandford 2009). We use horizon-penetrating Kerr-Schild coordinates for the Kerr metric (Gammie et al. 2003; McKinney & Gammie 2004), which avoids any issues with the coordinate singularity in Boyer-Lindquist coordinates. The code uses uniform internal coordinates  $(t, x^{(1)}, x^{(2)}, x^{(3)})$  mapped to the physical coordinates  $(t, r, \theta, \phi)$ . The radial grid mapping is

$$r(x^{(1)}) = R_0 + \exp(x^{(1)}), \quad (7)$$

which spans from  $R_{\text{in}} = 0.9r_H$  to  $R_{\text{out}} = 200M$ , where  $r_H$  is the radius of the outer event horizon. This just ensures the grid never extends inside the inner horizon, in which case the equations of motion would no longer be hyperbolic. The parameter  $R_0 = 0.3M$  controls the resolution near the horizon. For the outer radial boundary of the box, absorbing (outflow, no inflow allowed) boundary conditions are used.

The  $\theta$ -grid mapping is

$$\theta(x^{(2)}) = \left[ Y(2x^{(2)} - 1) + (1 - Y)(2x^{(2)} - 1)^7 + 1 \right] (\pi/2), \quad (8)$$

where  $x^{(2)}$  ranges from 0 to 1 (i.e. no cut-out at the poles) and  $Y = 0.65$  is chosen to concentrate grid zones

toward the equator. Reflecting boundary conditions are used at the polar axes. The  $\phi$ -grid mapping is given by  $\phi(x^{(3)}) = 2\pi x^{(3)}$ , such that  $x^{(3)}$  varies from 0 to 1/2 for a box with  $\Delta\phi = \pi$ . Periodic boundary conditions are used in the  $\phi$ -direction. Penna et al. (2010) considered various  $\Delta\phi$  for thin disks and found little difference in the results. In all of their tests,  $\Delta\phi > 7|h/r|$  and we remain above this limit as well. In what follows, spatial integrals are renormalized to refer to the full  $2\pi$  range in  $\phi$ , even if our computational box size is limited in the  $\phi$ -direction. For the purpose of radiative transfer we combine two identical regions of size  $\Delta\phi = \pi$  preserving the orientation to obtain the span of full  $2\pi$ .

### 3.4. Resolution and Spatial Convergence

The resolution of the simulations is  $N_r \times N_\theta \times N_\phi = 256 \times 64 \times 32$ . This is the fiducial resolution of Penna et al. (2010). Shafee et al. (2008) found this resolution to be sufficient to obtain convergence compared to a similar  $512 \times 128 \times 32$  model. In the vertical direction, we have about 7 grid cells per density scale height. Turbulence is powered by the MRI, which is seeded by the vertical component of the magnetic field (Balbus & Hawley 1998). The characteristic length scale of the MRI is the wavelength of the fastest growing mode:

$$\lambda_{\text{MRI}} = 2\pi \frac{v_A^z}{\Omega_0}, \quad (9)$$

where  $v_A^z$  is the vertical component of the Alfvén speed. We find that the MRI is well-resolved in the midplane of disk both initially and in the saturated state.

Penna et al. (2010) studied convergence in  $N_r$ ,  $N_\theta$ , and  $N_\phi$  and found that models with  $N_r = 256$  or  $N_r = 512$ ,  $N_\theta = 64$  or  $N_\theta = 128$ , and  $N_\phi = 64$  or  $N_\phi = 32$  behaved similarly for disks with similar resolution across the disk. Our resolution of the MRI and prior convergence testing by Penna et al. (2010) for similarly-resolved disks justify our choice of grid resolution. It is currently not computationally feasible to perform a similar spin parameter study at much higher resolutions, and future studies will continue to explore whether such simulations are fully converged (Hawley et al. 2011).

### 3.5. Ceiling constraints

During the simulation, the rest-mass density and internal energy densities can become low beyond the corona, but the code remains accurate and stable for a finite value of  $b^2/\rho$ ,  $b^2/u_g$ , and  $u_g/\rho$  for any given resolution. We enforce  $b^2/\rho \lesssim 10$ ,  $b^2/u_g \lesssim 100$ , and  $u_g/\rho \lesssim 10$  by injecting a sufficient amount of mass or internal energy into a fixed zero angular momentum observer (ZAMO) frame with 4-velocity  $u_\mu = \{-\alpha, 0, 0, 0\}$ , where  $\alpha = 1/\sqrt{-g^{tt}}$  is the lapse.

We have checked that the ceilings are rarely activated in the regions of interest of the flow. Figure 2 shows the constrained ratios,  $b^2/\rho$ ,  $b^2/u_g$ , and  $u_g/\rho$ , as a function of  $\theta$  at six radii ( $r = 4, 6, 8, 10, 12$ , and  $14M$ ) for the  $a_* = 0$  model. The data has been time-averaged over the steady state period from  $t = 14000M$  to  $200000M$ . The ceiling constraints are shown as dashed red lines. The solution stays well away from the ceilings. Thus, the ceilings are sufficiently high.

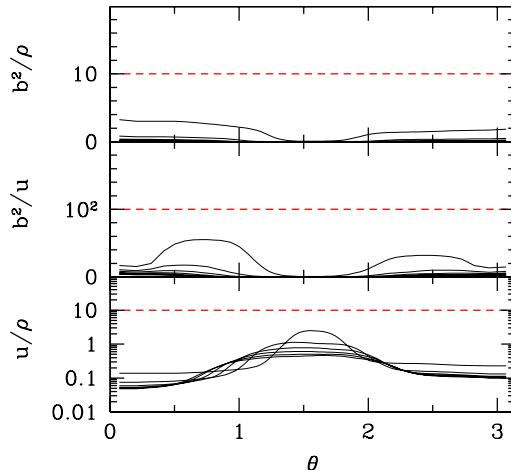


**Figure 2.** Ratios of  $b^2/\rho$ ,  $b^2/u_g$ , and  $u_g/\rho$  versus  $\theta$ . Black curves correspond to different radii in the flow; from top to bottom,  $r = 4, 6, 8, 10, 12$ , and  $14M$ . The data is time-averaged over the steady state period of the flow, from  $t = 14000M$  to  $20000M$ . Numerical ceilings constrain the solution to lie below the dashed red lines, but we see that the solution does not approach these limits.

### 3.6. Temporal Convergence

We run the simulations from  $t = 0M$  to  $t = 20000M$ . The accretion rate, the height- and  $\phi$ -averaged plasma  $\beta$ , and other disk parameters, fluctuate turbulently about their mean values. The simulation reaches a quasi-steady state, when the mean parameter value are time-independent. Figure 3 shows the accretion rate and height- and  $\phi$ -averaged  $\beta$  at the event horizon as a function of time for all five models. We take the period from  $t = 14000M$  to  $t = 20000M$  to define steady state.

As shown in Penna et al. (2010), for disk models like the one considered, the disk outside the innermost stable circular orbit (ISCO) behaves like the  $\alpha$ -disk model with  $\alpha \sim 0.1$  across disk thicknesses of  $h/r \sim 0.05 - 0.4$ . This allows one to accurately infer the timescale for reaching “inflow equilibrium,” corresponding to a quasi-steady flow across all quantities, at a given radius. For  $h/r \sim 0.3$  by  $t \sim 15000M - 20000M$  (the simulation runs till  $20000M$ , but the initial  $5000M$  are transients not necessarily associated with achieving inflow equilibrium for a simple viscous disk), we use the results in Appendix B of Penna et al. (2010) and find that inflow equilibrium is achieved within a radius of  $r \sim 25M - 30M$  for models with  $a_* \sim 1$  and  $r \sim 35M$  for models with  $a_* \sim 0$ . Even for a doubling of the viscous timescale, inflow equilibrium is achieved by  $r \sim 20M - 25M$  depending upon the BH spin. This motivates using an analytical extension of the simulation solution for radii beyond  $r \sim 25M$  as described later in § 4.1.

### 3.7. Evolved disk structure

Figure 4 shows matter stream lines as vectors and number density  $n_e$  as greyscale map. The large scale vortices existing on a single time shot (panel a) almost disappear, when averaged over  $6000M$  (panel b) in between  $14000M$  and  $20000M$ . The density is the highest in the equatorial plane on average, but deviations are present on the instantaneous map. The ISCO does not have any

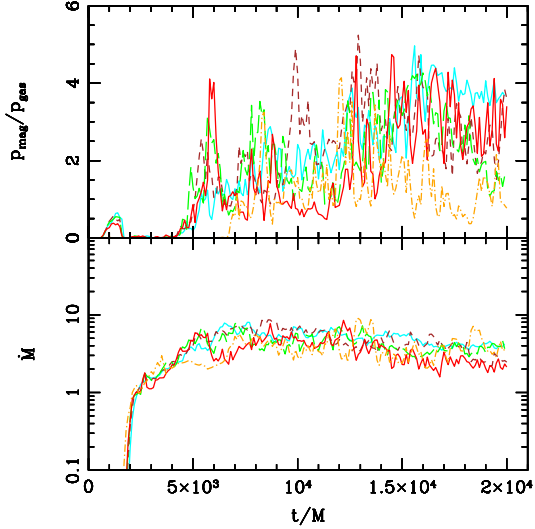


**Figure 3.** Accretion rate and height- and  $\phi$ -averaged  $\beta$  versus time at the event horizon for all five models:  $a_* = 0$  (solid light cyan),  $a_* = 0.5$  (solid dark red),  $a_* = 0.7$  (long-dashed green),  $a_* = 0.9$  (short-dashed brown), and  $a_* = 0.98$  (dot-dashed orange).

special significance: density and internal energy density increase through ISCO towards the BH horizon.

Figure 5 shows magnetic field lines as vectors and comoving electromagnetic energy density  $\propto b^2$  as a greyscale map. The structure of magnetic field at early times remembers the initial multi-loop field geometry (Penna et al. 2010), but switches at late times to a helical magnetic field structure resembling a split-monopole in meridional projection. Such switching of magnetic field structure suggests that final helix with projected split monopole is as a natural outcome of any vertical flux being dragged into the BH. The magnetic field structure of a single snapshot (panel a) looks similar to the structure of the linear average between 14000M and 20000M (panel b). The polar region of the flow has the strongest magnetic field.

#### 4. DYNAMICAL MODEL BASED ON SIMULATIONS

We now discuss extensions of the numerical simulation which we need to perform radiative transfer computations. We extend the simulations to large radii and define the electron temperature.

##### 4.1. Extension to large radii

The flow is evolved in a quasi-steady state for 6000M, from 14000M until 20000M, which corresponds to 8 orbits at  $r = 25M$ . The flow is not sufficiently settled at larger radii, however, and some Faraday rotation may happen and some emission might occur outside 25M. So we extend the dynamical model to larger radii  $r > 25M$  in a continuous way and check in Appendix A, how variations of our large radius prescriptions change the results of radiative transfer. The boundary of radiative transfer is situated at  $r = 20000M$ . The profiles of number density  $n_e$ , internal energy density  $u_g$ , magnetic field  $\mathbf{b}$  and velocity  $\mathbf{v}$  are extended as power-laws until radius  $r = 20000M$ . The power-law index for number density  $\beta$  is obtained by matching the known value  $n_e = 130\text{cm}^{-3}$  at about  $1.5'' \approx 3 \cdot 10^5 M$  (Baganoff et al. 2003) and the average  $n_{e,\text{cut}}$  value at  $r = 25M$  in the

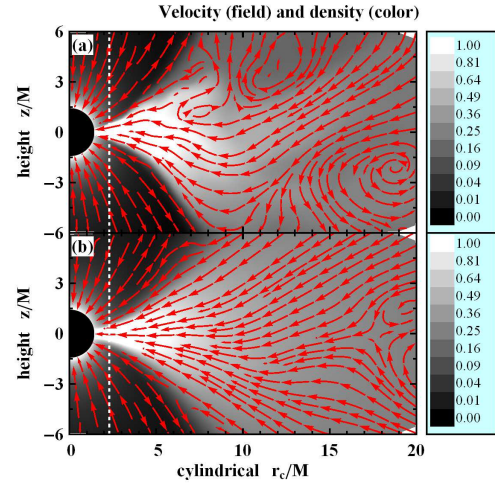


**Figure 4.** Stream lines of velocity (red vectors) and number density  $n_e$  (greyscale map) for spin  $a_* = 0.9$  at  $\phi = 0$  in the meridional plane: single time snapshot at  $t = 14000M$  on the upper (a) panel and time average between  $t = 14000M$  and  $t = 20000M$  on the lower (b) panel. The corresponding calibration bars of  $n_e$  are shown on the right. Number density is normalized by its maximum value.

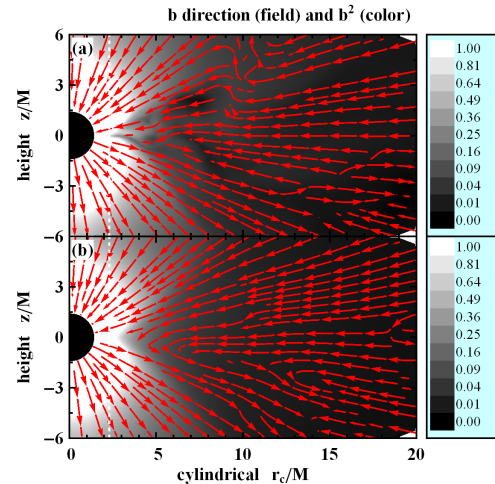


**Figure 5.** Magnetic field lines (red vectors) and comoving electromagnetic energy density  $\propto b^2$  (greyscale map) for spin  $a_* = 0.9$  at  $\phi = 0$  in the meridional plane ( $r_c$  as cylindrical radius): single time snapshot at  $t = 14000M$  on the upper (a) panel and time average between  $t = 14000M$  and  $t = 20000M$  on the lower (b) panel. The corresponding calibration bars of comoving  $b^2$  are shown on the right. Magnetic field energy density is normalized by its maximum value.

equatorial plane for each model. The value of  $\beta$  may be different for different models. The radial flow velocity  $v_r$  is then obtained from the continuity relation in the equatorial plane  $n_e v_r r^2 = \text{const}$ . The power-law of internal energy density  $u_g$  is obtained in a similar way by matching the values  $T_e = T_p = 1.5 \cdot 10^7$  K and  $n_e = 130\text{cm}^{-3}$  at distance  $3 \cdot 10^5 M$  (Baganoff et al. 2003; Shcherbakov & Baganoff 2010). The extensions of other flow velocities and magnetic field are fixed. The meridional physical velocity is extended as  $v_{\hat{\theta}} \propto (r/M)^{-3/2}$ , toroidal as  $v_{\hat{\phi}} \propto (r/M)^{-1/2}$  to approximately match the power law between 15M and 25M, where the relationship

$v_i \approx u^i \sqrt{g_{ii}}$  is used to connect the 4-velocity components with physical velocity components. All components of comoving magnetic field are extended as  $b_r, b_\theta, b_\phi \propto (r/M)^{-1}$ . This power-law slope corresponds roughly to equipartition magnetic field energy density, since constant fraction magnetic field is  $b \propto \sqrt{nT_p} \propto (r/M)^{-1}$  for  $n \propto (r/M)^{-1}$ . Exploration of various extensions of the magnetic field will be the topic of future studies.

After defining the extension power-laws for quantities in the equatorial plane, we extend the quantities radially at arbitrary  $\theta$  and  $\phi$  in a continuous way. For example, for density at arbitrary  $\theta$  and  $\phi$  and at  $r > 25M$  we have

$$n_e(r, \theta, \phi) = n_e(25M, \theta, \phi) \left( \frac{r}{25M} \right)^{-\beta}, \quad (10)$$

where  $n_e(25M, \theta, \phi)$  is taken from the simulations. We similarly extend other quantities. As we will show in Appendix A, small variations in power-law indices of number density and temperature have little influence on radiation intensities, linear and circular polarization fluxes, whereas variations of magnetic field slope can make a substantial difference.

#### 4.2. Electron temperature

Neither the proton  $T_p$  nor the electron  $T_e$  temperature is given directly by the simulations. However, it is crucial to know the electron temperature  $T_e$  to determine the emission. Our solution is to split the total internal energy density  $u_g$ , given by the simulations and their power-law extension, between the proton energy and the electron energy. The energy balance states

$$\frac{u_g}{\rho} \equiv \frac{u_{p,g} + u_{e,g}}{\rho} = c_p k_B T_p + c_e k_B T_e, \quad (11)$$

where  $c_p = 3/2$  and  $c_e \geq 3/2$  are the respective heat capacities,  $\rho$  is the rest-mass density, and  $k_B$  is Boltzmann's constant. The difference of temperatures  $T_p - T_e$  is influenced by three effects: equilibration by Coulomb collisions at large radii, the difference in heating rates  $f_p$  and  $f_e$  of protons and electrons operating at intermediate radii, and the difference in heat capacities operating close to the BH. Radiative cooling is ignored since, according to Sharma et al. (2007), the radiative efficiency of the flow is negligible for realistic  $\dot{M} \lesssim 10^{-7} M_\odot \text{year}^{-1}$ . The relevant effects can be summarized by the equation:

$$v_r \frac{d(T_p - T_e)}{dr} = -\nu_c (T_p - T_e) + \left( \frac{1}{c_p} \frac{f_p}{f_p + f_e} - \frac{1}{c'_e} \frac{f_e}{f_p + f_e} \right) v_r \frac{d(u_g/\rho)}{k_B dr}, \quad (12)$$

where

$$\nu_c = 8.9 \cdot 10^{-11} \left( \frac{T_e}{3 \cdot 10^{10}} \right)^{-3/2} \frac{n_e}{10^7} \quad (13)$$

is the non-relativistic temperature equilibration rate by collisions (Shkarofsky et al. 1966), all quantities being measured in CGS units. We consider protons to always have non-relativistic heat capacity and collisions to always obey the non-relativistic formula. The magnitudes of errors introduced by these simplification are negligible. The exact expressions for total electron heat capacity and

differential heat capacity are approximated as

$$c_e = \frac{u_{e,g}/\rho}{k_B T_e} \approx \frac{3}{2} \frac{0.7 + 2\theta_e}{0.7 + \theta_e}, \quad (14)$$

$$c'_e = \frac{d(u_{e,g}/\rho)}{k_B dT_e} \approx 3 - \frac{0.735}{(0.7 + \theta_e)^2} \quad (15)$$

correspondingly with the error  $< 1.3\%$ , where

$$\theta_e = \frac{k_B T_e}{m_e c^2} \quad (16)$$

is the dimensionless electron temperature. It was recently shown (Sharma et al. 2007) that the ratio of heating rates in the non-relativistic regime in a disk can be approximated as

$$\frac{f_e}{f_p} = C \sqrt{\frac{T_e}{T_p}} \quad (17)$$

with coefficient  $C$ . This formula is adopted in the relativistic regime as well, since no better prescription is available. Sharma et al. (2007) found the value  $C = 0.33$  in simulations, whereas we find  $C = 0.37 - 0.41$  for the best-fitting models (see § 7). The proton and electron temperatures are determined at each point in the following way. We first take a single snapshot of a simulation with spin  $a_*$  and extend the quantities to  $r = 20000M$  (see § 4.1). Then we compute azimuthal averages of radial velocity  $v_r$ , number density  $n_e$ , and  $u_g/\rho$  at the equatorial plane, extend them as power laws to  $r_{\text{out}} = 3 \cdot 10^5 M$ , and solve the equations (11,12) from  $r_{\text{out}}$  down to the inner grid cell point. Temperatures are set to  $T_e = T_p = 1.5 \cdot 10^7$  K at  $r_{\text{out}}$  (Baganoff et al. 2003; Shcherbakov & Baganoff 2010). On the next step we compare the values of  $u_g/\rho$  to the calculated  $T_e$  and  $T_p$  and determine the functional dependence  $T_e = T_e(u_g/\rho)$  and  $T_p = T_p(u_g/\rho)$ . At each point of the simulation (including off the equator), we draw temperatures from this correspondence. Typical profiles of proton and electron temperatures are shown on Figure 6. Temperatures stay equal until  $r \sim 10^4 M$  due to collisions, despite different heating prescriptions. Within  $r = 3 \cdot 10^3 M$  the timescale of collisional equilibration becomes relatively long and electrons become relativistic, thus  $T_e$  drops down below  $T_p$ . We take the inner part within  $r < 20000M$  of the electron and proton temperature profiles to conduct the radiative transfer.

For a given accretion rate there exists a unique dependence of the ratio of temperatures  $T_p/T_e$  at  $6M$  on the heating coefficient  $C$ .

## 5. GENERAL RELATIVISTIC POLARIZED RADIATIVE TRANSFER

Now we convert the dynamical model of the accretion flow into a set of observable quantities using polarized radiative transfer (Broderick et al. 2009; Shcherbakov & Huang 2011). We closely follow Shcherbakov & Huang (2011) for the transfer technique. Similarly to Huang et al. (2009a), we define the polarized basis in the picture plane, where one vector points North, another vector points East, and the wavevector points towards the observer. We parallel transport this basis in the direction of the BH and do the radiative transfer along the ray in the opposite direction. At each

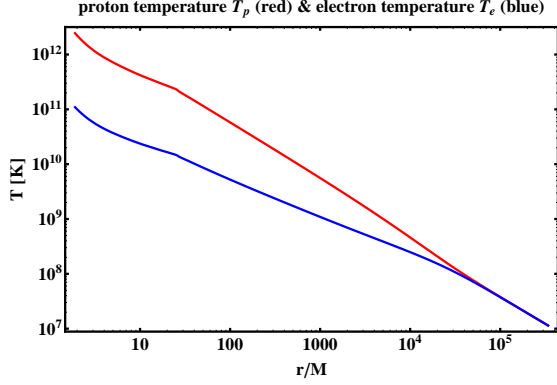


**Figure 6.** Temperatures of protons  $T_p$  (upper red line) and electrons  $T_e$  (lower blue line) as functions of radius for heating parameter  $C = 0.390$  and accretion rate  $\dot{M} = 4.6 \times 10^{-8} M_\odot \text{year}^{-1}$ , which leads to  $T_p/T_e = 19.0$  and  $T_e = 3.3 \cdot 10^{10}$  K at  $r = 6M$ . The dynamical model with this heating prescription, this accretion rate, and spin  $a_* = 0.5$  provides the fit with the lowest  $\chi^2$  to polarization observations (see § 7).

point along the ray we go to the locally-flat comoving frame, calculate the angles between the magnetic field and basis vectors, and compute the Faraday conversion, Faraday rotation, emissivities, and absorptivities.

Our calculation of plasma response is different from Shcherbakov & Huang (2011). That paper offered a way to find exact emissivities, absorptivities, Faraday rotation, and conversion coefficients for thermal and other isotropic particle distributions. Here, for simplicity, we employ fitting formulas for Faraday rotation and Faraday conversion and synchrotron approximation for emissivities in thermal plasma. We define

$$X = \frac{2}{3} \frac{\nu}{\nu_B \gamma^2 \sin \theta_B}, \quad (18)$$

where  $\theta_B$  is  $\mathbf{k}\text{-}\mathbf{b}$  angle,  $\gamma$  is electron gamma factor, and  $\nu_B = eb/(2\pi m_e c)$  is the cyclotron frequency. Then following Legg & Westfold (1968); Melrose (1971), we write down emissivities in the  $I$ ,  $Q$ , and  $V$  modes as

$$\begin{aligned} \varepsilon_I &= \frac{\sqrt{3}}{2} \frac{e^2}{c} \nu_B \sin \theta_B \int_1^{+\infty} d\gamma N(\gamma) X \int_X^{+\infty} dz K_{5/3}(z), \\ \varepsilon_Q &= \frac{\sqrt{3}}{2} \frac{e^2}{c} \nu_B \sin \theta_B \int_1^{+\infty} d\gamma N(\gamma) X K_{2/3}(X), \\ \varepsilon_V &= \frac{2}{\sqrt{3}} \frac{e^2}{c} \nu_B \cos \theta_B \int_1^{+\infty} d\gamma \frac{N(\gamma)}{\gamma} \times \\ &\quad \times \left[ X K_{1/3}(X) + \int_X^{+\infty} dz K_{1/3}(z) \right]. \end{aligned} \quad (19)$$

Here  $K_z(x)$  is the Bessel function of the 2nd kind of order  $z$ . We employed IEEE/IAU definitions of Stokes  $Q$ ,  $U$ , and  $V$  (Hamaker & Bregman 1996), also chosen in Shcherbakov & Huang (2011): counter-clockwise rotation of electric field as seen by the observer corresponds to positive  $V > 0$ . Under this definition the sign of  $V$  emissivity (19) is opposite to the sign in Rybicki & Lightman (1967). A variation of emissivity formulas (18,19) exists: Sazonov (1969); Pacholczyk (1970) define  $X = 2\nu/(3\nu_B(\gamma - 1)^2 \sin \theta_B)$ , integrating over particle energy instead of  $\gamma$ . This approximation

appears to give significantly larger errors at low particle energies.

Next, one needs to specify which particle distribution  $N(\gamma)$  to use. Various  $N(\gamma)$  correspond to various synchrotron approximations for thermal plasmas. The ultrarelativistic approximation (Pacholczyk 1970; Huang et al. 2009a) with  $N(\gamma) = \exp(-\gamma/\theta_e)(\gamma - 1)^2/2/\theta_e^3$  gives the simplest distribution. However, the exact thermal distribution of particles

$$N(\gamma) = \gamma \sqrt{\gamma^2 - 1} \frac{\exp(-\gamma/\theta_e)}{\theta_e K_2(\theta_e^{-1})} \quad (20)$$

allows for more precise computation of radiation. Synchrotron emissivities based on the equations (18,19) with the exact thermal distribution (20) agree with the exact cyclo-synchrotron emissivities  $\varepsilon_I$ ,  $\varepsilon_Q$ , and  $\varepsilon_V$  (Leung, Gammie & Noble 2011; Shcherbakov & Huang 2011) to within 2% for typical dynamical models and frequencies  $> 100$  GHz. Emissivities integrated over the ultrarelativistic thermal distribution typically have  $\sim 10\%$  error.

Thermal absorptivities are found from emissivities (19) via Kirchoff's law

$$\alpha_{I,Q,V} = \varepsilon_{I,Q,V}/B_\nu, \quad (21)$$

where  $B_\nu = 2k_B T_e \nu^2/c^2$  is the source function for low photon energies  $h\nu \ll k_B T_e$ . Faraday rotation  $\rho_V$  and Faraday conversion  $\rho_Q$  coefficients are taken from Shcherbakov (2008):

$$\begin{aligned} \rho_V &= g(Z) \frac{2n_e e^2 \nu_B}{m_e c \nu^2} \frac{K_0(\theta_e^{-1})}{K_2(\theta_e^{-1})} \cos \theta, \\ \rho_Q &= f(Z) \frac{n_e e^2 \nu_B^2}{m_e c \nu^3} \left[ \frac{K_1(\theta_e^{-1})}{K_2(\theta_e^{-1})} + 6\theta_e \right] \sin^2 \theta. \end{aligned} \quad (22)$$

Here

$$Z = \theta_e \sqrt{\sqrt{2} \sin \theta} \left( 10^3 \frac{\nu_B}{\nu} \right) \quad (23)$$

and

$$\begin{aligned} g(Z) &= 1 - 0.11 \ln(1 + 0.035Z), \\ f(Z) &= 2.011 \exp\left(-\frac{Z^{1.035}}{4.7}\right) - \\ &\quad - \cos\left(\frac{Z}{2}\right) \exp\left(-\frac{Z^{1.2}}{2.73}\right) - 0.011 \exp\left(-\frac{Z}{47.2}\right) \end{aligned} \quad (24)$$

are the fitting formulas for deviations of  $\rho_V$  and  $\rho_Q$  from analytic results for finite ratios  $\nu_B/\nu$ . The deviation of  $f(Z)$  from 1 is significant for the set of observed frequencies  $\nu$ , temperatures  $\theta_e$ , and magnetic fields found in the typical models of Sgr A\*. These formulas constitute a good fit to the exact result for the typical parameters of the dynamical model (Shcherbakov 2008).

Polarized radiative transfer can take much longer to perform compared to non-polarized radiative transfer when using an explicit integration scheme to evolve the Stokes occupation numbers  $N_Q$ ,  $N_U$ , and  $N_V$ . Large Faraday rotation measure and Faraday conversion measure lead to oscillations between occupation numbers. One of the solutions is to use an implicit integration

scheme, while another solution is to perform a substitution of variables. In the simple case of Faraday rotation leading to interchange of  $N_Q$  and  $N_U$ , our choice of variables is the amplitude of oscillations and the phase. Thus the cylindrical polarized coordinates arise

$$\begin{aligned} N_Q &= N_{QU} \cos \phi, \\ N_U &= N_{QU} \sin \phi. \end{aligned} \quad (25)$$

Then the amplitude  $N_{QU}$  slowly changes along the ray and the angle  $\phi$  changes linearly, which translates into speed improvement. In the presence of substantial Faraday conversion, the polarization vector precesses along some axis in Poincaré sphere, adding an interchange of circularly and linearly polarized light. Polar polarized coordinates would be more suitable in this case:

$$\begin{aligned} N_Q &= N_{\text{pol}} \cos \phi \sin \psi, \\ N_U &= N_{\text{pol}} \sin \phi \sin \psi, \\ N_V &= N_{\text{pol}} \cos \psi, \end{aligned} \quad (26)$$

where  $N_{\text{pol}}$  is the total polarized intensity, the change of  $\phi$  angle is mainly due to Faraday rotation and  $\psi$  angle changes owing to Faraday conversion. The application of this technique speeds up the code enormously at low frequencies  $\nu < 100$  GHz.

Besides improving the speed, we perform a number of convergence tests to make sure the final intensities are precisely computed. Radiative transfer involves shooting a uniform grid of  $N \times N$  geodesics from the picture plane. Even though  $N = 150$  (Dexter et al. 2009) may be a better number to use for a single snapshot,  $N = 111$  works well for a series of many snapshots giving an accuracy of  $\chi_H^2/\text{dof} < 0.01$  near the best-fitting models. The metrics of relative integration error  $\chi_H^2/\text{dof}$  is defined in Appendix A, where the convergence tests are described. The shape of the integration domain is taken to be a square in the picture plane with a side

$$a[M] = 16 + 2 \left( \frac{600}{\nu[\text{GHz}]} \right)^{1.5} \quad (27)$$

in the units of  $r_g \equiv M$ , where frequency  $\nu$  is in GHz. The size based on formula (27) is larger than the photon orbit visible diameter  $d_{\text{ph}} \approx 10.4M$  at the same time following the intrinsic size dependence on frequency (Shen et al. 2005; Doeleman et al. 2008) at low frequencies. Justification of this size by convergence tests is given in Appendix A. An important radiative transfer parameter is the distance from the BH, where intensity integration starts. The dependence of synchrotron emissivity on temperature and magnetic field strength is so strong that it negates the effect of gravitational redshift close to the BH. The accuracy of  $\chi_H^2/\text{dof} < 0.02$  is achieved in sub-mm for computation out from  $r_{\text{min}} = 1.01r_H$ , where  $r_H = M(1 + \sqrt{1 - a_*^2})$  is the horizon radius (see Appendix A).

## 6. STATISTICAL ANALYSIS

We now use statistical analysis to discriminate between models. We consider all available observations and explore models with 4 parameters: spin  $a_*$ , inclination angle  $\theta$ , accretion rate  $\dot{M}$ , ratio of proton to electron temperature  $T_p/T_e$  at  $6M$ . For the radiative transfer calcu-

lations, the density in simulations is scaled to give the desired accretion rate.

As indicated in Section 2, the samples of total fluxes, LP and EVPA at high frequencies are consistent with a Gaussian distribution so we can directly apply  $\chi^2$  statistics. We compare the means of observed variable fluxes to the means of fluxes computed over several simulation snapshots. The number of simulation snapshots in this work is 11. We define  $\chi_F^2$  for fitting total fluxes as

$$\chi_F^2 = \sum_{i=1}^7 \frac{(F_{i,\text{sim}} - F_{i,\text{obs}})^2}{\sigma(F)^2}, \quad (28)$$

for the set of 7 frequencies  $\nu = 88, 102, 145, 230, 349, 680,$  and  $857$  GHz, where  $\sigma_F$  are the errors of the means. We incorporate LP fractions at 88, 230, and 349 GHz and CP fraction at 230 and 349 GHz to obtain the full  $\chi^2$ :

$$\begin{aligned} \chi^2 &= \chi_F^2 + \sum_{i=1}^3 \frac{(\text{LP}_{i,\text{sim}} - \text{LP}_{i,\text{obs}})^2}{\sigma(\text{LP})^2} \\ &+ \sum_{i=1}^2 \frac{(\text{CP}_{i,\text{sim}} - \text{CP}_{i,\text{obs}})^2}{\sigma(\text{CP})^2}. \end{aligned} \quad (29)$$

Then we take the number of degrees of freedom to be  $\text{dof}_F = 7 - 3 = 4$  for flux fitting and  $\text{dof} = 12 - 3 = 9$  for fitting all polarized data. We compute the probability density  $\rho(\chi^2) = \rho(\chi^2|a_*, \theta, \dot{M}, C)$  of the data, given a model, from the corresponding  $\chi^2$  distributions. This is a function of spin, inclination angle, accretion rate, and heating coefficient. Now the search for minimum  $\chi^2$  is fully defined. The probability density of model given data  $\rho(a_*, \theta, \dot{M}, C|\chi^2)$  is needed for confidence intervals calculation. It is found by Bayes' theorem with the use of priors (Broderick et al. 2009)

$$\rho(a_*, \theta, \dot{M}, C|\chi^2) = \frac{\rho(\chi^2)\pi(\theta)\pi(\dot{M})\pi(C)}{\int \rho(\chi^2)\pi(\theta)\pi(\dot{M})\pi(C)d\theta d\dot{M} dC}, \quad (30)$$

where we assumed a separable prior  $\pi(\theta, \dot{M}, C) = \pi(\theta)\pi(\dot{M})\pi(C)$ . We expect no preferred spin orientation, which requires a uniform distribution over the solid angle and the prior  $\pi(\theta) = \sin \theta$ . The probability density  $\rho(a_*, \theta, \dot{M}, C|\chi^2)$  is considered independently for each spin, since we cannot integrate over spin having 5 values of  $a_*$ . The accretion rate  $\dot{M}$  is largely uncertain. For our analysis we take the logarithmic prior  $\pi(\dot{M}) = \dot{M}^{-1}$ , which is the best non-informative prior for a large range of possible values (Jaynes & Bretthorst 2003). The value of the heating coefficient  $C = 0.33$  cited by Sharma et al. (2007) was based on a small part of total energy dissipation and may be unreliable. A similar prior  $\pi(C) = C^{-1}$  can be taken for the heating coefficient. The expectation value of any quantity  $Q$  at certain spin  $a_*$  is calculated as the integral

$$\langle Q_{a_*} \rangle = \iiint Q \rho(a_*, \theta, \dot{M}, C|\chi^2) \sin \theta d\theta \frac{dC}{C} \frac{d\dot{M}}{\dot{M}}, \quad (31)$$

and the confidence intervals are found analogously.

We explore the values of  $C$  from 0.20 to 0.75, which leads to  $T_p/T_e$  at  $6M$  between 6 and 60. All models

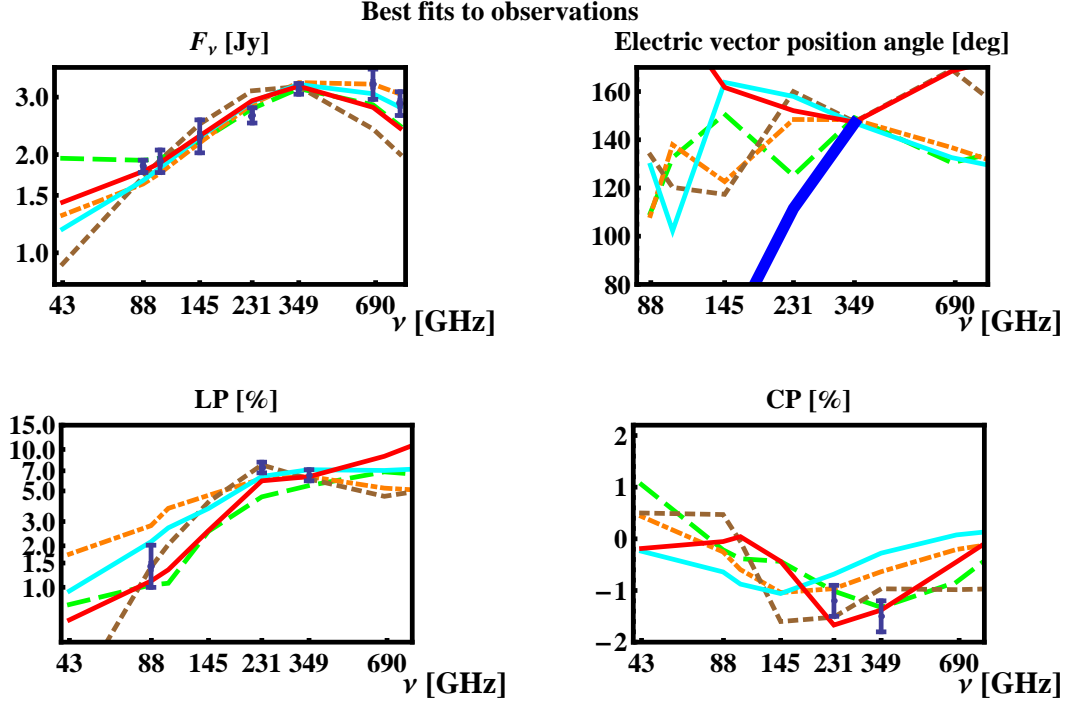


**Figure 7.** Best fits to the observed fluxes, LP and CP fractions by best models for each spin. The inclination angle  $\theta$ , accretion rate  $\dot{M}$ , ratio of temperatures  $T_p/T_e$  were adjusted for each spin to minimize  $\chi^2$ . Fits to total flux  $F_\nu$  are in the upper left panel, LP fraction in the lower left, and CP fraction in the lower right. The best model with spin  $a_* = 0.5$  (solid dark red) has  $\chi^2/\text{dof} = 2.09$ , spin  $a_* = 0.7$  (long-dashed green) —  $\chi^2/\text{dof} = 3.31$ , spin  $a_* = 0.9$  (solid light cyan) —  $\chi^2/\text{dof} = 3.91$ , spin  $a_* = 0.98$  (dot-dashed orange) —  $\chi^2/\text{dof} = 3.71$ , spin  $a_* = 0$  (short-dashed brown) —  $\chi^2/\text{dof} = 4.48$ . The upper left panel shows the dependence of EVPA angle on frequency for the best models. Note, that EVPA angles are not included into our  $\chi^2$  fitting procedure. The thick blue curve represents observations. Simulated EVPA curves are arbitrarily shifted to approximate EVPA at 349 GHz. The addition of an external (to the emitting region) Faraday rotation screen helps to fit EVPA(349 GHz) – EVPA(230 GHz).

with fixed  $C = 0.20$ , which provide the best fits to total fluxes, under-predict the linear polarization at all frequencies. Similarly, all models with  $C = 0.75$ , which fit total fluxes, over-predict the linear polarization. So we cover all relevant models by using this wide range of  $C$ .

A full analysis in the space of accretion rate  $\dot{M}$  is not possible due to limited computational resources. Instead, for each spin  $a_*$ , heating coefficient  $C$ , and inclination  $\theta$  we find  $\dot{M}$ , which gives the best  $\chi^2_F$  for the values of flux  $F_\nu$  (see eq.28) and explore close-by  $\dot{M}$ . As the dependence of total flux on accretion rate is uniform, this guarantees that we explore all regions with low full  $\chi^2$  defined by equation (29). Even if there is some good fit to LP and CP curves, but the flux values are either over-predicted or under-predicted, then the total  $\chi^2/\text{dof}$  would be substantially larger than unity.

## 7. RESULTS

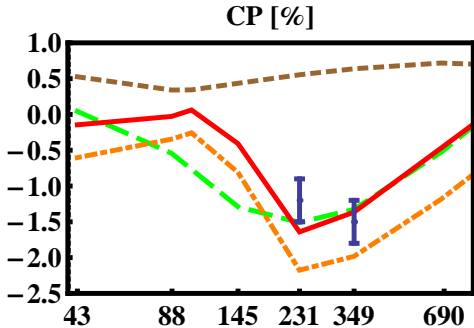
In previous sections we described observations, numerical simulations of the dynamical structure, prescription for electron temperature, polarized radiative transfer, and statistical methods to compare the simulated spectra with the observations. We now fit the observations with  $\chi^2/\text{dof} \sim 2$  and constrain some model parameters.

Figure 7 shows best fits to observations by models with five different spins. Inclination angle  $\theta$ , accretion rate  $\dot{M}$ , heating coefficient  $C$  were adjusted to reach the lowest  $\chi^2$ . The best model with spin  $a_* = 0.5$  (solid dark red) has  $\chi^2/\text{dof} = 2.09$ , spin  $a_* = 0.7$  (long-dashed green)

—  $\chi^2/\text{dof} = 3.31$ , spin  $a_* = 0.9$  (solid light cyan) —  $\chi^2/\text{dof} = 3.91$ , spin  $a_* = 0.98$  (dot-dashed orange) —  $\chi^2/\text{dof} = 3.71$ , spin  $a_* = 0$  (short-dashed brown) —  $\chi^2/\text{dof} = 4.48$ .

Fits to fluxes  $F_\nu$  (upper left) are not substantially different, though models with higher spins perform better at high frequencies. Larger deviations can be seen on LP (lower left) and CP (lower right) plots. Models with high spins require lower accretion rate/density to fit the flux spectrum. Then they are not subject to Faraday depolarization, which leads to decrease of LP at low  $\nu$ , and the models end up having larger linear polarization fractions at 88 GHz. Not all models reproduce the observed decrease of mean LP fraction between 230 GHz and 349 GHz groups. The discrepancies in fitting CP fraction are also large: all lowest- $\chi^2$  models give  $|\text{CP}| < 1.5\%$  at 349 GHz. The best model with spin  $a_* = 0$  reproduces LP and CP fractions well, but fails in fitting the total flux. Most solutions predict the wrong sign of the EVPA(349 GHz)–EVPA(230 GHz) difference, which can be fixed with stronger magnetic field to yield stronger Faraday rotation as demonstrated on Figure 7. The best model with spin  $a_* = 0.5$  has inclination angle  $\theta = 64^\circ$ , mean accretion rate  $\dot{M} = 4.6 \times 10^{-8} M_\odot \text{year}^{-1}$ , ratio of temperatures  $T_p/T_e = 19.0$  at  $6M$ , which gives  $T_e = 3.3 \cdot 10^{10}$  K at that distance from the center in equatorial plane. The best models with other high spins give similar inclination angles:  $\theta = 57^\circ, 57^\circ, 59^\circ$  at  $a_* = 0.7, 0.9, 0.98$ , respectively.

Let us now isolate the physical effects responsible for the observed polarized quantities. Several comparable



**Figure 8.** Contributions of different effects to CP fraction as a function of frequency for best-fitting  $a_* = 0.5$  model. Shown are observations (blue error bars), the best fit model (solid red line), the same dynamical model computed with zero V emissivity  $\varepsilon_V = 0$  in radiative transfer so that CP is produced by Faraday conversion (dot-dashed orange), the same model with zero Faraday conversion  $\rho_Q = 0$  (short-dashed brown), and the same model with zero Faraday rotation  $\rho_V = 0$  (long-dashed green). Emissivity in circular V mode contributes little to the observed CP, which is mainly due to Faraday conversion.

in strength radiative transfer effects may account for observed polarized fluxes. Let us consider the production of circular polarization in the flow. Figure 8 shows the consequences of switching various physical effects off for the best-fitting model with spin  $a_* = 0.5$ . The solid curve is the result with all physics on. The dot-dashed orange line below is produced, when circular emissivity is set to  $\varepsilon_V = 0$ . The brown dashed line corresponds to zero Faraday conversion ( $\rho_Q = 0$ ). Switching off  $\varepsilon_V$  emissivity leads to a minor correction, whereas setting Faraday conversion to zero results in several times smaller CP of a different sign. So most of the CP in this model is produced by Faraday conversion. It would be incorrect, however, to think that the simple linear to circular conversion explains the observed CP. The dashed green line in Figure 8 shows the CP fraction, when Faraday rotation is switched off ( $\rho_V = 0$ ). The effect of Faraday rotation is insignificant at  $\nu > 150$  GHz, but the rotation of the plane of linear polarization simultaneous with conversion between linear and circular polarizations produces a unique effect at lower  $\nu$ . This is the so-called “rotation-induced conversion” (Homan et al. 2009). Possible sign oscillations of V with frequency do not happen, whether or not Faraday rotation is involved.

In Figure 9 we illustrate the influence of Faraday rotation on LP fraction (left panel) and EVPA angle (right panel). The solid curves are produced with all physics on for the best model with spin  $a_* = 0.5$ . The green dashed lines are computed for switched off Faraday rotation ( $\rho_V = 0$ ). The Faraday rotation is negligible at high frequencies and LP curves look similar at  $\nu > 200$  GHz. As the rotation of polarization plane is much stronger at low  $\nu$ , a significant phase shift accumulates between different rays at the low end of the spectrum and cancellations of LP become strong at  $\nu < 150$  GHz. This illustrates the effect of Faraday depolarization (Bower et al. 1999a). In the absence of Faraday rotation the dependence of EVPA on frequency is not constant: the varia-

tions of intrinsic emitted EVPA are significant. Thus, the change of EVPA with  $\nu$  should not always be ascribed to the effect of Faraday rotation. The positive observed slope of EVPA with  $\nu$  at high  $\nu$ , acquired due to negative Faraday rotation measure  $RM < 0$ , is comparable to the slope of intrinsic emitted EVPA. The dot-dashed black lines correspond to the model, where the magnetic field slope is set to the shallower  $B \propto r^{-0.5}$  in the extension region  $r > 25M$ . This gives larger Faraday rotation far from the BH and essentially serves as an external Faraday rotation screen. The model leads to better agreement with EVPA curve and gives the correct sign of  $EVPA(349 \text{ GHz}) - EVPA(230 \text{ GHz})$ , but it still suffers a substantial beam depolarization and under-predicts LP at low frequencies.

Besides computing the best fit models, we examine regions of parameter space near those best fits in search for anomalies. For example, if there is a coincidental cancellation in one of the models, then the close-by models have much higher  $\chi^2/\text{dof}$  and such a best fit may be unreliable as it is accidental. In Figure 10 we plot the behavior of reduced  $\chi^2$  for models near the best-fitting model with spin  $a_* = 0.5$ . The upper row shows the contours of  $\chi_F^2/\text{dof}_F$  for flux fitting, whereas the lower row shows the contours of  $\chi^2/\text{dof}$  for fitting full polarization data. The left column shows the contours with changing accretion rate  $\dot{M}$  and ratio of temperatures  $T_p/T_e$  at  $6M$  at constant inclination angle  $\theta$ , whereas the right column shows contours with changing ratio of temperatures  $T_p/T_e$  at  $6M$  and inclination angle  $\theta$  at constant accretion rate. The contours of reduced  $\chi^2$  are color-coded from the highest (red) to the lowest (blue) values.

Plot of  $\chi_F^2/\text{dof}_F$  (panel (a)) reveals a significant degeneracy between the electron temperature and accretion rate: lower  $T_e$  and higher  $\dot{M}$  or higher  $T_e$  and lower  $\dot{M}$  both fit the flux well. This degeneracy breaks for the full  $\chi^2/\text{dof}$ , when fitting LP and CP, which fixes the matter density (panel (b)). Similarly, a large range of inclination angles gives a fit to  $\chi_F^2/\text{dof}_F$  (panel (c)). The range of possible  $\theta$  significantly shrinks, when all polarized fluxes are included into the fit (panel (d)). Panel (b) shows smooth contours of reduced  $\chi^2$ . The contours on panel (d) are not as smooth, but the polarization fractions depend sensitively on  $\theta$  changes. This indicates the absence of clear anomalies in the fit, so the fit does not seem to be accidental.

We illustrated in Figure 7 how the best-fitting models with different spins perform. Now we visualize in Figure 11 the differences between  $\chi^2/\text{dof}$  and  $\chi_F^2/\text{dof}_F$  for the best-fitting models. Blue curves on both panels show the total reduced  $\chi^2/\text{dof}$ , whereas red curves on the left panel correspond to  $\chi_F^2/\text{dof}_F$  for flux spectrum fitting. Panel (a) shows the best  $\chi_F^2/\text{dof}_F$  and  $\chi^2/\text{dof}$  as functions of spin  $a_*$ . We see that the best  $\chi_F^2/\text{dof}_F$  for flux fitting is below unity for high spins  $a_* = 0.7, 0.9, 0.98$ , whereas good fits cannot be achieved for the lowest spin  $a_* = 0$ . The best model with spin  $a_* = 0.5$  exhibits the lowest reduced  $\chi^2$ . However, the value  $\chi^2/\text{dof} = 2.09$  is not close to unity, which indicates significant room is available to improve the model. We illustrate the stability of the best fit in panel (b) of Figure 11. There we show the best  $\chi^2/\text{dof}$  for models with spin  $a_* = 0.5$  for various

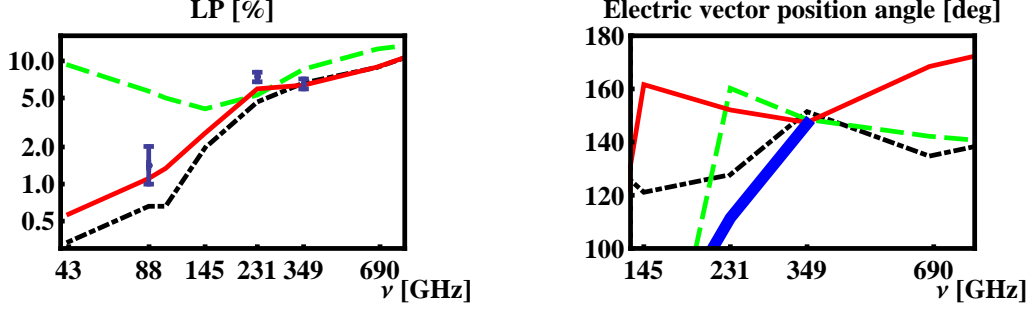


**Figure 9.** Contributions of different effects to LP fraction (on the left) and EVPA angle (on the right) as functions of frequency for the best-fitting spin  $a_* = 0.5$  model. Shown are observations (blue error bars and thick blue line), the best fit model (solid red line), the same dynamical model computed with zero Faraday rotation  $\rho_V = 0$  in radiative transfer (long-dashed green), and the same dynamical model with a shallow slope of magnetic field  $B \propto r^{-0.5}$  extension to large radii (dot-dashed black). Beam depolarization is weak, when Faraday rotation is absent: then LP stays high at low frequencies. Even when the Faraday rotation is set to zero, the observed EVPA depends on frequency due to varying intrinsic emission EVPA. Faraday rotation in the best-fitting model is too weak to reproduce EVPA observations, but stronger magnetic field at large radii leads to better agreement.

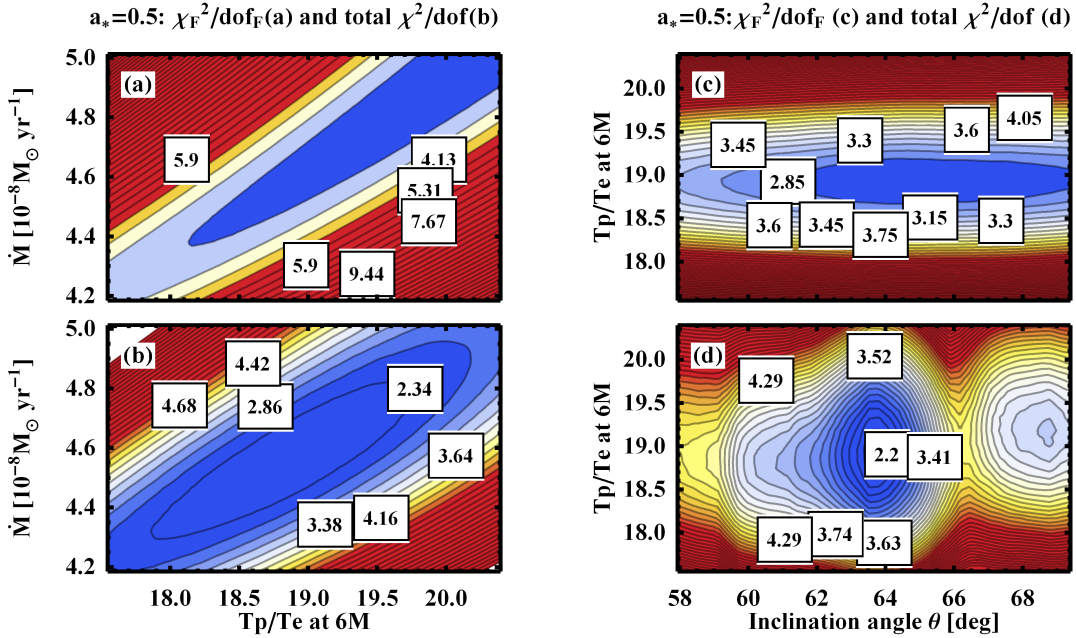


**Figure 10.** Behavior of  $\chi^2$  near the best-fitting model with spin  $a_* = 0.5$ : with changing accretion rate  $\dot{M}$  and ratio of temperatures  $T_p/T_e$  at  $6M$  (left column) and with changing ratio of temperatures  $T_p/T_e$  at  $6M$  and inclination angle of BH spin  $\theta$  (right column). Contours of  $\chi_F^2/\text{dof}_F$  for flux fitting are in the upper row, contours for full  $\chi^2/\text{dof}$  are in the lower row.

sets of snapshots, over which the radiation transfer is conducted. Our main model is based on 11 snapshots taken every 600M between 14,000M and 20,000M. The models depicted in panel (b) are based on 6 small intervals with 11 snapshots each taken every 100M: the intervals are centered at 14,500M, 15,500M, 16,500M, 17,500M, 18,500M, and 19,500M. The values of  $\chi^2/\text{dof}$  are depicted on panel (b) at the corresponding interval middles: 14,500M, 15,500M etc. The values of  $\chi^2/\text{dof}$  fluctuate between intervals by up to  $\Delta\chi^2/\text{dof} \sim 1$ , which is comparable to the difference  $\Delta\chi^2/\text{dof} = 1.6$  between best spin  $a_* = 0.5$  and spin  $a_* = 0.98$  models. Thus, we can conclude that the model with spin  $a_* = 0.5$  is marginally better than the models with spins  $a_* = 0, 0.7, 0.9, 0.98$ .

Changes of best  $\chi^2/\text{dof}$  with time interval show a small secular trend, which may indicate secular changes in accretion rate or magnetic field structure (however, see Section 3.6 for the discussion of convergence).

There is another way to test the dynamical models against observations. The intrinsic image size was recently measured (Doeleman et al. 2008) with the VLBI technique. The measured correlated flux at 230 GHz was  $F_{\text{corr}} \approx 0.35$  Jy at 3.5 G $\lambda$  SMT-JCMT baseline. Similar values of correlated flux were observed later by the same group (Fish et al. 2011). We plot this correlated flux with  $3\sigma$  error bar in Figure 12 and compare it to simulated correlated fluxes, normalizing the total flux to the mean observed  $F_\nu = 2.64$  Jy. To simulate the correlated flux we follow Fish et al. (2009) and em-

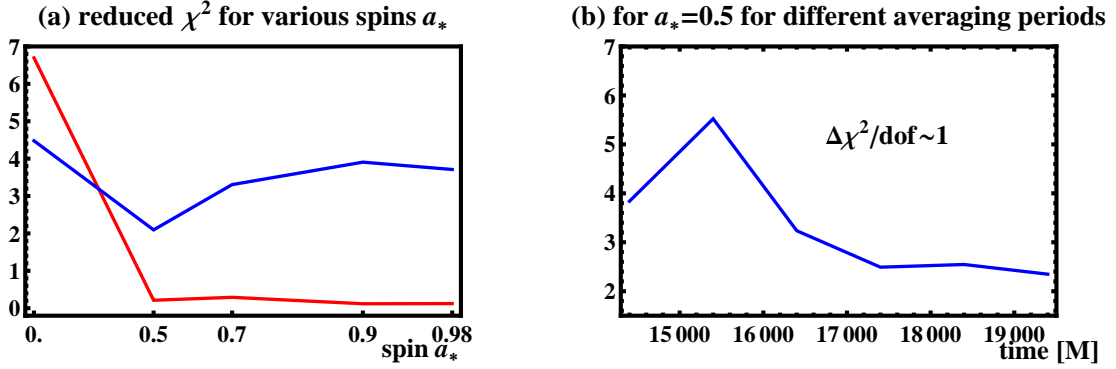


**Figure 11.** The lowest reduced  $\chi^2$  for fits with each spin  $a_*$ . Blue upper curve on panel (a) corresponds to total  $\chi^2/\text{dof}$  for fitting total flux at 7 frequencies, LP fraction at 3 frequencies, and CP fraction at 2 frequencies. Red lower curve corresponds to  $\chi^2_F/\text{dof}_F$  for fitting total flux at 7 frequencies. Best reduced  $\chi^2$  for spins  $a_* = 0, 0.5, 0.7, 0.9, 0.98$  is shown on panel (a) for simulated fluxes averaged over 11 snapshots taken every  $600M$  within the period  $14000 - 20000M$ . Spin  $a_* = 0.5$  gives the lowest reduced  $\chi^2$ . Best reduced  $\chi^2$  for spin  $a_* = 0.5$  is shown on panel (b) for simulated fluxes averaged over smaller intervals within  $14000 - 20000M$  time range. We take 6 such intervals with 11 snapshots taken every  $100M$ : the intervals are centered at  $14500M, 15500M, 16500M, 17500M, 18500M, \text{ and } 19500M$ . The variations of  $\chi^2/\text{dof}$  between intervals are large reaching  $\pm 1$ .

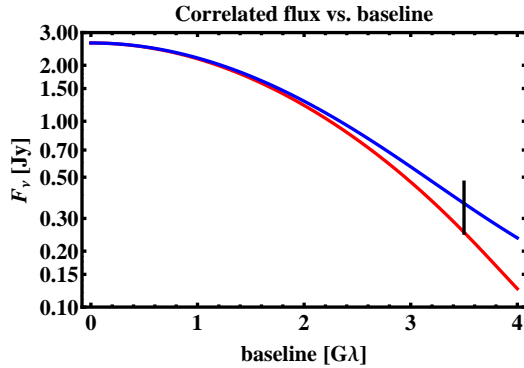


**Figure 12.** Correlated flux as a function of baseline at 230 GHz normalized to average observed flux 2.64 Jy for best-fitting model with spin  $a_* = 0.5$ . The upper line shows the smallest size (largest correlated flux) over all position angles of BH spin axis, the lower line shows the largest size (smallest correlated flux) over all position angles. An observation presented in Doeleman et al. (2008) with  $3\sigma$  error bars at baseline 3.5 G $\lambda$  is drawn for comparison.

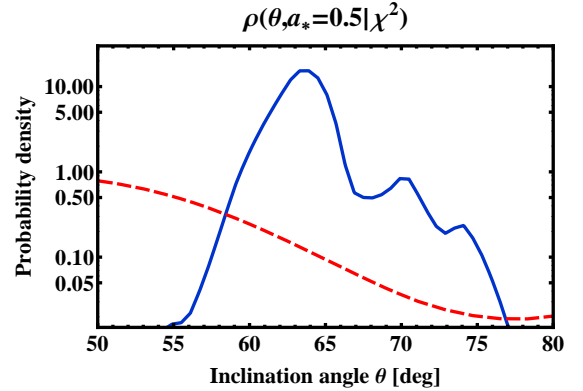


**Figure 13.** Probability density  $\rho(\theta, a_* = 0.5 | \chi^2)$  of inclination angle  $\theta$  for spin  $a_* = 0.5$  marginalized over the heating parameter  $C$  and accretion rate  $\dot{M}$ . Shown are probability density for full polarized fitting (blue solid line) and for fitting the total flux spectrum (dashed red curve). The corresponding 90% confidence interval  $\theta = 60^\circ - 69^\circ$  for full polarized fitting is very narrow owing to high sensitivity of polarization fractions to inclination angle. The fitting of only flux spectrum leaves the inclination angle poorly constrained.

ploy a Gaussian interstellar scattering ellipse with half-widths at half-maximum  $7.0 \times 3.8G\lambda$  with position angle  $170^\circ$  east of north. We vary the position angle (PA) of BH spin and plot correlated flux curves with the largest (blue upper line) and the smallest (red lower line) correlated flux at  $3.5G\lambda$ . The correlated fluxes for spin  $a_* = 0.5$  best-fitting model are shown. Since we do not fit EVPA directly, models with different PA have the same reduced  $\chi^2$ . The size in our best model with spin  $a_* = 0.5$  is marginally consistent with observations, but the correlated flux is slightly under-produced, which indicates the size of the shadow is slightly over-predicted. Fish et al. (2011) reported shadows of larger size than in Doeleman et al. (2008), the actual size may in fact agree with our best model. We discuss other possible ways to reconcile observations and simulations in the next section.

Having analyzed the best fits and compared the reduced  $\chi^2$ , we can estimate of the model parameters. Let us start with the inclination angle of BH spin  $\theta$  ( $\theta = 90^\circ$  for the edge-on disk). In Figure 13 we plot probability density  $\rho(\theta, a_* = 0.5 | \chi^2)$  for inclination angle for models with spin  $a_* = 0.5$ . This quantity represents probability

density of the model given the data (30) integrated over heating coefficient and accretion rate

$$\rho(\theta, a_* = 0.5 | \chi^2) \propto \iint \rho(a_* = 0.5, \theta, \dot{M}, C | \chi^2) \sin \theta \frac{dC}{C} \frac{d\dot{M}}{\dot{M}}. \quad (32)$$

The curve is normalized to give  $\int \rho(\theta, a_* = 0.5 | \chi^2) d\theta = 1$ . The corresponding central 90% confidence interval of  $\theta$  is

$$\theta_{\text{est}} = 60^\circ - 69^\circ. \quad (33)$$

The probable range of  $\theta$  is small in the model, which gives tight constraints on  $\theta$  assuming spin  $a_* = 0.5$  is the true spin. The best  $\theta$  for other high spins  $a_* = 0.7, 0.9, 0.98$  are about  $57^\circ - 59^\circ$ . This suggests that the computed confidence interval may give a good estimate of a true inclination angle in Sgr A\* system. Likewise, we can calculate 90% confidence intervals for electron temperature  $T_e$  at  $6M$  for spin  $a_* = 0.5$  models:

$$T_e = (3.4 - 4.2) \cdot 10^{10} \text{ K}. \quad (34)$$

The accretion rate  $\dot{M}$  has a similar width

$$\dot{M}_{\text{est}} = (3.8 - 5.0) \times 10^{-8} M_{\odot} \text{year}^{-1}. \quad (35)$$

There is one more quantity we can estimate: the position angle (PA) of BH spin. Similarly to Huang et al. (2009a), we rely on observed intrinsic EVPA  $\approx 111.5^{\circ}$  at 230 GHz and EVPA  $\approx 146.9^{\circ}$  at 349 GHz (see § 2). For the model to fit the difference in EVPA, we add a Faraday rotation screen far from the BH with constant rotation measure (RM). Then we compute the required RM and the intrinsic PA to fit the simulated EVPA at 230 and 349 GHz. The best-fitting model with  $a_* = 0.5$  gives PA =  $89^{\circ}$  East of North, whereas the best-fitting linear-averaged model with spin  $a_* = 0.9$  requires PA =  $122^{\circ}$ . The corresponding 90% confidence interval for spin  $a_* = 0.5$  models is

$$\text{PA}(\text{est}) = 69^{\circ} - 109^{\circ},$$

where the error is dominated by the observational error of EVPA determination (see Table 1). The estimated position still has large uncertainty, what precludes us from tightening the size estimates (see Figure 12) from the models. We employ the minimum and maximum correlated fluxes found over all orientations.

With the estimated orientation of the BH spin, we can plot an image of average radiation intensity from near the event horizon. Figure 14 shows images of total intensity  $I_{\nu}$  for the spin  $a_* = 0.5$  best-fitting solution (upper left panel), the spin  $a_* = 0.9$  best-fitting (lower left panel); LP intensity and CP intensity plots for best spin  $a_* = 0.5$  model (upper right and lower right panels, correspondingly). LP average intensity plot was made by averaging  $U$  and  $Q$  intensities separately and then finding the total LP fraction and EVPA angle. Blue (predominant) color on CP plot depicts the regions with negative CP intensity and red (subdominant) color depicts the regions with positive CP intensity. The total  $V$  flux from this solution is negative ( $V < 0$ ). The streamlines on LP plot are aligned with EVPA direction at each point. The spin axis is rotated by PA =  $89^{\circ}$  east of north for spin  $a_* = 0.5$  best solution and by PA =  $122^{\circ}$  for spin  $a_* = 0.9$  best solution. The spin axis is inclined at  $\theta$  to the line of sight, so that the either right (west) or left (east) portions of the flow are closer to the observer. The color schemes on all plots are nonlinear with corresponding calibration bars plotted on the sides. The numbers at the top of calibration bars denote normalizations.

## 8. DISCUSSION AND CONCLUSIONS

Let us compare our results with estimates of Sgr A\* accretion flow and BH parameters made by other groups. Two separate searches for spin based on GR numerical simulations have been reported so far: Moscibrodzka et al. (2009) and Dexter et al. (2010). The first paper browses the set of spins from  $a_* = 0.5$  to  $a_* = 0.98$  for 2D GRMHD simulations, fits X-Ray flux, 230 GHz flux, and slope at this frequency, and finds at least one model for each spin consistent with observations (see Table 3 therein). Their best-bet model has  $a_* = 0.9$ . Dexter et al. (2010) focuses on a set of 3D GRMHD, fits 230 GHz flux and size estimates and provides the table of spin probabilities with  $a_* = 0.9$  again having the highest  $P(a)$ . If we were to consider spectrum

fitting, then our results would conform to the picture with high spin  $a_* \sim 0.9$  being most likely. When we fit spectrum, LP and CP fractions, spin  $a_* = 0.5$  solutions give lower reduced  $\chi^2$  instead. We are unable to provide narrow constraints on  $a$ , and neither do other groups. Other spin estimates have been based on analytic models. Broderick et al. (2009, 2010) favor  $a_* = 0$  solutions, while Huang et al. (2009b) favor  $a_* < 0.9$  although they do not explore their full model parameter space. Another poorly constrained quantity is the accretion rate. Our estimate  $\dot{M}_{\text{est}} = (3.8 - 5.0) \cdot 10^{-8} M_{\odot} \text{year}^{-1}$  is broad. Good models in Moscibrodzka et al. (2009) give  $\dot{M}$  from  $0.9 \cdot 10^{-8} M_{\odot} \text{year}^{-1}$  to  $12 \cdot 10^{-8} M_{\odot} \text{year}^{-1}$ , which agrees with our range. Dexter et al. (2010) found relatively tight boundaries for 90% confidence interval of  $\dot{M}$  by looking at spin  $a_* = 0.9$  solutions by incorporating flow size in  $\chi^2$  analysis. Our estimates give much higher accretion than the range  $\dot{M} = 5_{-2}^{+15} \times 10^{-9} M_{\odot} \text{year}^{-1}$  (90%) in Dexter et al. (2010), since models with lower spin naturally need higher  $\dot{M}$  to fit the data. Note, that Dexter et al. (2009) found even lower accretion rate  $\dot{M}(0.9) = (1.0 - 2.3) \times 10^{-9} M_{\odot} \text{year}^{-1}$  because they assumed the proton and electron temperatures were identical.

In addition to spin and accretion rate we can try to constrain inclination angle  $\theta$  and electron temperature  $T_e$  at  $6M$ . Our estimate is  $\theta_{\text{est}} = 60^{\circ} - 69^{\circ}$ , which is the narrowest of all estimates in the literature. This  $\theta$  is marginally consistent with the estimates  $\theta = 50^{\circ}$  in Broderick et al. (2009); Dexter et al. (2010). Huang et al. (2009a) and Huang et al. (2009b) favor slightly lower  $\theta = 40^{\circ}, 45^{\circ}$ , but have large error bars. Inclusion of polarized observations also puts stricter limits on  $T_e$ . Moscibrodzka et al. (2009) and Dexter et al. (2010) set constant  $T_p/T_e$ , whereas Huang et al. (2009a) and the present work calculate the profile of  $T_e$ . In all models,  $T_e$  is a shallow function of radius, which made Dexter et al. (2010) estimate the “common”  $T_e = (5.4 \pm 3.0) \times 10^{10}$  K, which is the quantity calculated supposedly still at certain distance from the BH center. Setting this distance to  $6M$  we arrive at the consistent, but narrower conservative estimate  $T_{e,\text{est}} = (3.4 - 4.2) \times 10^{10}$  K. There are two kinds of constraints on BH spin position angle: 230 GHz correlated flux fitting and EVPA fitting. The first path was adopted in Broderick et al. (2009) and Dexter et al. (2010) with the results PA =  $(-20^{\circ}) - (-70^{\circ}) = (110^{\circ}) - (180^{\circ})$ . The polarization data gives slightly different results. Meyer et al. (2007) predicts the range PA =  $60^{\circ} - 108^{\circ}$ , whereas Huang gets either PA  $\approx 115^{\circ}$  (Huang et al. 2009b) or PA  $\approx 140^{\circ}$  (Huang et al. 2009a) depending on the model without calculating the range. Our estimate of PA =  $69^{\circ} - 109^{\circ}$  is narrow, and agrees with Meyer et al. (2007). Significantly larger error bars, and the fact that very few size observations are available, make PA estimates from size less reliable than those from EVPA. In addition, the size of the flow may depend substantially on luminosity state (Broderick et al. 2009) or the presence of non-thermal structures, spiral waves, and other features. In some astrophysical sources PA is directly known from spatially resolved jets, and Sgr A\* may be one of such sources. A tentative jet feature was revealed in X-rays

images of total and polarized intensities for best-fitting models

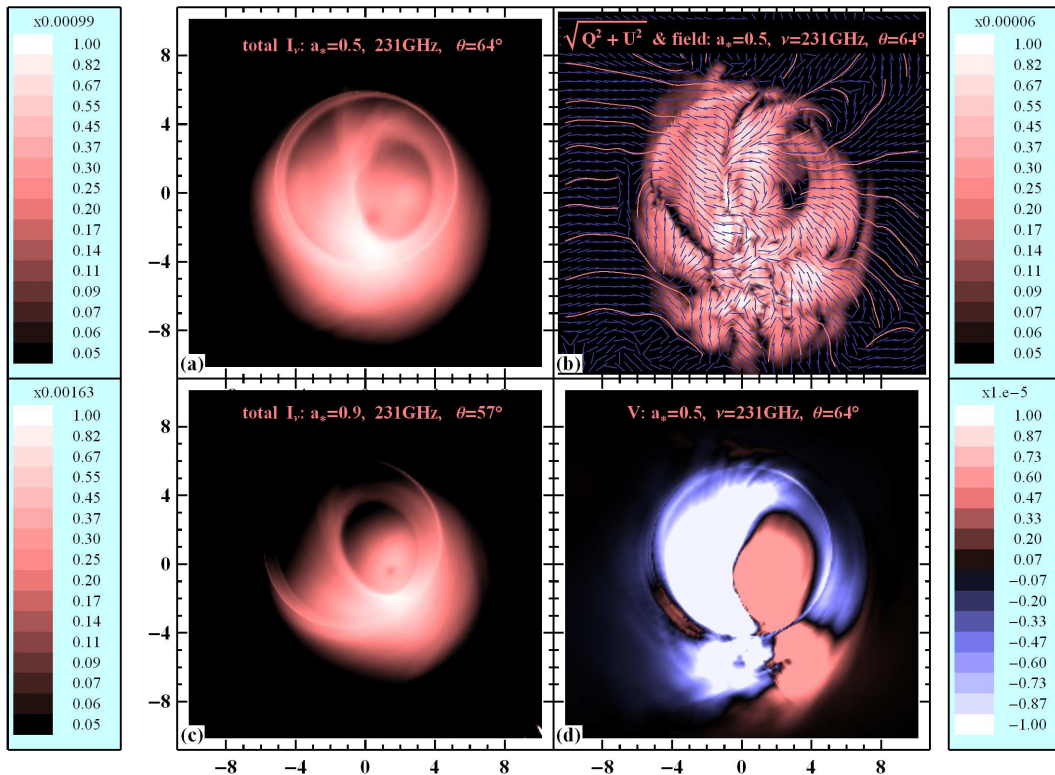


**Figure 14.** Images of polarized intensities for the best-fitting models: total intensity for spin  $a_* = 0.9$  model (lower left); intensities for  $a_* = 0.5$  model: total intensity (upper left), linear polarized intensity and streamlines along EVPA (upper right), and circular polarized intensity (lower right). Distances are in the units of BH mass  $M$ . Images are rotated in the picture plane to correspond to the best spin PA: PA =  $89^\circ$  for  $a_* = 0.5$  model and PA =  $122^\circ$  for  $a_* = 0.9$  model. Individual calibration bars are on the sides of corresponding plots. The ill-defined polar region does not contribute significantly to the emission.

by Munro et al. (2008), Fig. 8 with  $\text{PA}_{\text{jet}} = 120^\circ$ . This value lies outside of our present 90% confidence interval, however.

Besides the estimates of accretion rate and flow properties based on the inner flow, there exist estimates based on the outer flow. Shcherbakov & Baganoff (2010) constructed an inflow-outflow model with conduction and stellar winds, which agreed to X-ray surface brightness profile observed by *Chandra*. Their model had an accretion rate  $\dot{M} = 6 \cdot 10^{-8} M_\odot \text{year}^{-1}$  and electron temperature  $T_e = 3.6 \times 10^{10}$  K at  $6M$  from the center, which shows a great agreement with present results. So the radial extensions of density to large radius is justified. Shcherbakov & Baganoff (2010) constrain density in the outer flow from X-ray observations and the present work constrains it in the inner flow from sub-mm observations. The density profile is found to be

$$\rho \propto r^{-\beta}, \quad \beta = 0.80 - 0.90 \quad (36)$$

is a narrow estimate. Density power-law index  $\beta$  lies between  $\beta = 1.5$  for ADAF flow (Narayan & Yi 1995) and  $\beta = 0.5$  for the convection-dominated accretion flow (Narayan, Igumenshchev, & Abramowicz 2000; Quataert & Gruzinov 2000). However, the modification of the power-law index from the steep ADAF profile

is likely due to conduction for Sgr A\*, not convection (Shcherbakov & Baganoff 2010).

Our dynamical model makes several approximations. The slopes of density  $n_e$  and temperatures  $T_p$  and  $T_e$ , fixed at the outer flow, break at a  $25M$  radius, where the power law radial extrapolation starts. Future simulations will need to cover a larger range of radii and potentially add conduction (Johnson & Quataert 2007; Sharma et al. 2008; Shcherbakov & Baganoff 2010). Simulations with larger outer radial boundaries and run for longer times will also help to constrain the Faraday rotation, which happens for the present models partially outside of the simulated domain. The proper simulation of the polar region of the flow may be important as well. At present we artificially limit magnetization and temperature there. If we do not, then numerical artifacts associated with excessive numerical dissipation and heating appear, similar to those in Moscibrodzka et al. (2009).

We favor  $a_* = 0.5$ , whereas other groups find  $a_* = 0$  and  $a_* = 0.9$  are the best fits to their models. So there is no consensus on the spin of Sgr A\* at present. A shortcoming is the use of thermal distributions. If the non-thermal electrons provide most of the energy for the sub-mm peak, then this would invalidate the spin estimates (Shcherbakov & Huang 2011).

Radiative transfer has its own assumptions. Our emissivities in the special synchrotron approximation

<sup>4</sup> Note that gravitational radius is defined as  $r_g = 2M$  in Shcherbakov & Baganoff (2010).

provide e.g. 2% agreement with exact emissivities (Leung, Gammie & Noble 2011; Shcherbakov & Huang 2011) for  $b = 20$  G,  $\theta_B = 1$  rad,  $T_e = 6.9 \cdot 10^9$  K, and observed frequency  $\nu = 100$  GHz. Agreement is better for larger  $T_e$ . The non-polarized radiative transfer of total intensity (Moscibrodzka et al. 2009; Dexter et al. 2010) has an intrinsic error in comparison with polarized radiative transfer with the same total emissivity  $\varepsilon_I$ , however the error is 1 – 5%.

There are still unaccounted for sources of error. The mass of the BH in the Galactic Center is known to within 10% (Ghez et al. 2008) and the distance is known to 5%. We do not expect these uncertainties to lead to significant changes in our predictions. A shift to slightly lower spin may be able to mimic the effect of smaller BH or a BH at larger distance from us.

The reduced  $\chi^2$ -based analysis has its problems. For example, the true number of the degrees of freedom in a non-linear fitting (Andrae et al. 2010) may not coincide with the number of observation types minus the number of free parameters. Simultaneous observations at different frequencies may give correlated fluxes, which would lead to lower dof. Then the computed reduced  $\chi^2/dof$  should be considered as a lower boundary to the true reduced  $\chi^2/dof$ . However, often observations over which the means are computed are not simultaneous. The means at different frequencies are not expected to be correlated for non-simultaneous observations. A careful evaluation of correlations should be done in the future.

Apart from questions of modeling, the improvement of observational data can lead to further insights on the flow structure and more reliable estimates of BH spin. The detailed comparison of flux, LP, and CP curves in Figure 7 shows that the models with spin  $a_* = 0.5$  and spin  $a_* = 0.9$  have discrepancies in regions not constrained by observations. In particular, the CP fractions at 145 GHz are different. EVPA data needs improvement as well. Despite some statistics available at 230 GHz and 349 GHz, the variability of EVPA is about  $20^\circ$ , which translates to  $\pm 20^\circ$  ( $3\sigma$ ) uncertainty of the mean PA, whereas the modeling uncertainty is several degrees. More observations of EVPA at these frequencies will help to find the Faraday rotation measure more precisely and constraint the PA of BH spin. An alternative is to observe at higher frequencies  $\nu \geq 690$  GHz, where both the Faraday rotation effect and fluctuations of the intrinsic emission EVPA are small. Another important quantity, LP at 88 GHz, has a largely unknown value. Its observations are reported in 2 papers. Variations in simulated LP(88GHz) are large between the best models (see Figure 7). Refinement of the observed mean LP(88GHz) could potentially help discriminate better between the  $a_* = 0.5$  and  $a_* = 0.9$  spin solutions. A measurement of the emitting region size or the correlated flux is also promising. Despite the correlated flux at 230 GHz being measured at the SMT-JCMT  $3.5G\lambda$  baseline, the statistics of this measurement are needed to capture variations of  $F_{\text{corr}}$  over at least a year to be comparable with the statistics of total flux. The correlated flux observations are currently being accumulated (Fish et al. 2011). The correlated flux at this baseline is exponentially sensitive to the physical flow size, which can make slightly brighter

states have significantly lower  $F_{\text{corr}}$ . As a caveat, the conclusion on image sizes may depend on the behavior of matter in the ill-defined polar regions. Our models do not exhibit significant emission from high latitudes at 230 GHz (see Figure 14) or anywhere above 88 GHz.

Future work should incorporate more statistics from recent polarized observations in the sub-mm. Future 3D GRMHD simulations will model more radially extended flows, account for ADAF/ADIOS type scale-heights of  $|h/r| \sim 0.9$ , and capture outflows. Adding Comptonization to the radiative transfer would be one way to test the quiescent X-ray luminosity  $L \approx 4 \cdot 10^{32} \text{erg s}^{-1}$  within 2 – 10 keV (Shcherbakov & Baganoff 2010). So far we have focused on the mean state and discarded the information of simultaneity. These data will be used in future analyses of observations to tighten the error bars. The time variability properties can be found from the simulations and compared to the observed ones. In particular, “jet lags” (Yusef-Zadeh et al. 2008; Maitra, Markoff & Falcke 2009) and quasi-periodic oscillations (QPOs) (Genzel et al. 2003; Eckart et al. 2006; Miyoshi 2010) should be investigated using the simulations.

## 9. ACKNOWLEDGEMENTS

The authors are grateful to Lei Huang for checking various emissivity prescriptions, to Ramesh Narayan for extensive discussions and comments, to Avi Loeb, Avery Broderick, James Moran, Alexander Tchekhovskoy, Cole Miller, Julian Krolik, Steven Cranmer for insightful comments and Jim Stone for encouragement with self-consistent radiative transfer. We thank the anonymous referee for extensive feedback, which helped to improve the manuscript. The numerical simulations and the radiative transfer calculations in this paper were partially run on the Odyssey cluster supported by the FAS Sciences Division Research Computing Group at Harvard, Deepthought cluster at the University of Maryland, and were partially supported by NSF through TeraGrid resources provided by NCSA (Abe), LONI (QueenBee), and NICS (Kraken) under grant numbers TG-AST080025N and TG-AST080026N. The paper is partially supported by NASA grants NNX08AX04H (RVS&Ramesh Narayan), NNX08AH32G (Ramesh Narayan), NASA Hubble Fellowship grant HST-HF-51298.01 (RVS), NSF Graduate Research Fellowship (RFP), and NASA Chandra Fellowship PF7-80048 (JCM).

## REFERENCES

- Aitken, D. K., Greaves, J., Chrysostomou, A., Jenness, T., Holland, W., Hough, J. H., Pierce-Price, D., Richer, J. 2000, *ApJ*, 534, 173
- An, T., Goss, W. M., Zhao, J.-H., Hong, X. Y., Roy, S., Rao, A. P., Shen, Z.-Q. 2005, *ApJ*, 634, 49
- Andrae, R., Schulze-Hartung, T., Melchior, P. 2010, *astro-ph/1012.3754*
- Baganoff, F. K., et al. 2001, *Nature*, 413, 45
- Baganoff, F. K., et al. 2003, *ApJ*, 591, 891
- Balbus, S. A., & Hawley, J. F. 1998, *Reviews of Modern Physics*, 70, 1
- Beckwith K., Hawley J. F., Krolik J. H., 2008a, *ApJ*, 678,1180
- Berger, J. O. 1985, “Statistical Decision Theory and Bayesian Analysis”, (New York: Springer-Verlag)
- Blandford, R. D., & Begelman, M. C. 1999, *MNRAS*, 303L, 1

- Bower, G. C., Falcke, H., Backer, D. C. 1999a, *ApJ*, 523, L29
- Bower, G. C., Wright, M. C. H., Backer, D. C., Falcke, H. 1999b, *ApJ*, 527, 851
- Bower, G. C., Wright, M. C. H., Falcke, H., Backer, D. C. 2001, *ApJ*, 555, 103
- Bower, G. C., Falcke, H., Sault, R. J., Backer, D. C. 2002, *ApJ*, 571, 843
- Bower, G. C., Wright, M. C. H., Falcke, H., Backer, D. C. 2003, *ApJ*, 588, 331
- Bower, G. C., Falcke, H., Wright, M. C., Backer, & Donald C. 2005, *ApJ*, 618, 29
- Broderick, A. E., Fish, V. L., Doeleman, S. S., Loeb, A. 2009, *ApJ*, 697, 45
- Broderick, A. E., Fish, V. L., Doeleman, S. S., Loeb, A. 2010, *astro-ph/1011.2770*
- Chakrabarti S. K., 1985a, *ApJ*, 288, 1
- Chakrabarti S. K., 1985b, *ApJ*, 294, 383
- Chan, C.-K., Liu, S., Fryer, C. L., Psaltis, D., O’zel, F., Rockefeller, G., Melia, Fulvio 2009, *ApJ*, 701, 521
- De Villiers J.-P., Hawley J. F., Krolik J. H., 2003, *ApJ*, 599, 1238
- Dexter, J., Agol, E., Fragile, P. C. 2009, *ApJ*, 703, 142
- Dexter, J., Agol, E., Fragile, P. C., McKinney, J. C. 2010, *ApJ*, 717, 1092
- Dolence, J. C., Gammie, C. F., Moscibrodzka, M., Leung, P. K. 2009, *ApJS*, 184, 387
- Doeleman S. S. et al 2001, *AJ*, 121, 2610
- Doeleman, S. S. et al. 2008, *Nature*, 455, 78
- Eckart, A., Schödel, R., Meyer, L., Trippe, S., Ott, T., Genzel, R. 2006, *A&A*, 455, 1
- Falcke, H., Goss, W. M., Matsuo, H., Teuben, P., Zhao, J.-H., Zylka, R. 1998, *ApJ*, 499, 731
- Fish, V. L., Broderick, A. E., Doeleman, S. S., Loeb, A. 2009, *ApJ*, 692, L14
- Fish, V. L., et al. 2011, *ApJ*, 727, 36
- Fragile, P. C., Lindner, C. C., Aninos, P., & Salmonson, J. D. 2009, *ApJ*, 691, 482
- Fuerst, S. V., Wu, K. 2004, *A&A*, 424, 733
- Gammie, C. F., McKinney, J. C., Toth, G. 2003, *ApJ*, 589, 444
- Gammie, C. F., Shapiro, S. L., McKinney, J. C. 2004, *ApJ*, 602, 312
- Ghez, A. M., et al. 2008, *ApJ*, 689, 1044
- Ghosh, S., & Mukhopadhyay, B. 2007, *ApJ*, 667, 367
- Genzel, R., Schödel, R., Ott, T., Eckart, A., Alexander, T., Lacombe, F., Rouan, D., Aschenbach B. 2003, *Nature*, 425, 934
- Goldston, J. E., Quataert, E., Igumenshchev, I. V. 2005, *ApJ*, 621, 785
- Hamaker J. P., Bregman J. D. 1996, *A & AS*, 117, 161
- Hawley, J. F., Guan, X., Krolik, J. H. 2011, *ApJ*, 738, 84
- Herrnstein, R. M., Zhao, J.-H., Bower, G. C., Goss, W. M. 2004, *AJ*, 127, 3399
- Hide, R., Palmer, T. N. 1982, *Geophys. and Astrophys. Fluid Dynamics*, 19, 301
- Homan, D. C., Lister, M. L., Aller, H. D., Aller, M. F., Wardle, J. F. C. 2009, *ApJ*, 696, 328
- Huang, L., Liu, S., Shen, Z.-Q., Cai, M. J., Li, H., & Fryer, C. L. 2008, *ApJ*, 676L, 119
- Huang, L., Liu, S., Shen, Z.-Q., Yuan, Y.-F., Cai, M. J., Li, H., & Fryer, C. L. 2009a, *ApJ*, 703, 557
- Huang, L., Takahashi, R., Shen, Z.-Q. 2009b, *ApJ*, 706, 960
- Igumenshchev, I. V. 2008, *ApJ*, 677, 317
- Jaynes, E. T., Bretthorst, G. L. 2003, "Probability Theory", (Cambridge: Cambridge University Press)
- Johnson, B. M., Quataert, E. 2007, *ApJ*, 660, 1273
- Komissarov S. S., McKinney J. C., 2007, *MNRAS*, 377, L49
- Krichbaum T. P. 1998, *A&A*, 335, L106
- Krichbaum, T. P., Graham, D. A., Bremer, M., Alef, W., Witzel, A., Zensus, J. A., Eckart, A. 2006, *JPhCS*, 54, 328
- Legg, M. P. C., Westfold, K. C., 1968, *ApJ*, 154, 499
- Leung, P. K., Gammie, C. F., Noble S. C. 2011, *ApJ*, 737, 21
- Li, J., Shen, Z.-Q., Miyazaki, A., Huang, L., Sault, R. J., Miyoshi, M., Tsuboi, M., Tsutsumi, T. 2008, *JPhCS*, 131, 2007
- Lo, K. Y., Shen, Z.-Q., Zhao, J.-H., Ho, P. T. P. 1998, *ApJ*, 508, L61
- Lu, R.-S., Krichbaum, T. P., Eckart, A., König, S., Kunneriath, D., Witzel, G., Witzel, A., Zensus, J. A. 2008, *JPhCS*, 131, 2059
- Macquart, J.-P., Bower, G. C., Wright, M. C. H., Backer, Donald C., Falcke, H. 2006, *ApJ*, 646, L111
- Mahadevan, R. 1998, *Nature*, 394, 651
- Maitra, D., Markoff, S., Falcke, H. 2009, *A&A*, 508, 13
- Marrone, D. P., Moran, J. M., Zhao, J.-H., Rao, R. 2006a, *JPhCS*, 54, 354
- Marrone, D. P., Moran, J. M., Zhao, J.-H., Rao, R. 2006b, *ApJ*, 640, 308
- Marrone, D. P., Moran, J. M., Zhao, J., & Rao R., 2007, *ApJ*, 654L, 57
- Marrone D. P., et al. 2008, *ApJ*, 682, 373
- Mauerhan, J. C., Morris, M., Walter, F., Baganoff, F. K. 2005, *ApJ*, 623, 25
- McKinney, J. C., & Gammie, C. F. 2004, *ApJ*, 611, 977
- McKinney, J. C. 2006, *MNRAS*, 367, 1797
- McKinney, J. C. 2006, *MNRAS*, 368, 1561
- McKinney, J. C., & Blandford, R. D. 2009, *MNRAS*, 394, L126
- McKinney J. C., Narayan R., 2007a, *MNRAS*, 375, 513
- McKinney J. C., Narayan R., 2007b, *MNRAS*, 375, 531
- Melrose, D. B. 1971, *Ap&SS*, 12, 172
- Meyer, L., Schödel, R., Eckart, A., Duschl, W. J., Karas, V., Dovčiak, M. 2007, *A&A*, 473, 707
- Mignone, A., McKinney, J. C. 2007, *MNRAS*, 378, 1118
- Miyazaki, A., Tsutsumi, T., Tsuboi, M. 2004, *ApJ*, 611, 97
- Miyoshi, M., Shen, Z.-Q., Oyama, T., Takahashi, R., Kato, Y. 2010, *astro-ph/0906.5511*
- Moscibrodzka, M., Gammie, C. F., Dolence, J. C., Shiokawa, H., Leung, P. K. 2009 *ApJ*, 706, 497
- Muno, M. P., et al. 2008, *ApJ*, 673, 251
- Munoz, D. J., Marrone, D. P., Moran, J. M. 2009, *Bulletin of the AAS*, 41, 761
- Munoz, D. J., Marrone, D. P.; Moran, J. M., Rao, R. 2011, *ApJ*, submitted
- Narayan, R., & Yi, I. 1995, *ApJ*, 452, 710
- Narayan, R., Yi, I., Mahadevan, R. 1995, *Nature*, 374, 623
- Narayan, R., Mahadevan, R., Grindlay, J. E., Popham, R. G., Gammie, C. 1998, *ApJ*, 492, 554
- Narayan, R., Igumenshchev, I. V., & Abramowicz, M. A. 2000, *ApJ*, 539, 798
- Noble, S. C., Gammie, C. F., McKinney, J. C., Del Zanna, L. 2006, *ApJ*, 641, 626
- Noble, S. C., Krolik, J. H. 2009, *ApJ*, 703, 964
- Özel, F., Psaltis, D., Narayan, R. 2000, *ApJ*, 541, 234
- Pacholczyk, A. G. 1970, "Radio astrophysics. Nonthermal processes in galactic and extragalactic sources", (Freeman: San Francisco)
- Penna, R. F., McKinney, J. C., Narayan, R., Tchekhovskoy, A., Shafee, R., McClintock, J. E. 2010, *MNRAS*, 408, 752
- Quataert, E., & Gruzinov, A. 2000, *ApJ*, 539, 809d
- Reid, M. J., Broderick, A. E., Loeb, A., Honma, M., Brunthaler, A. 2008, *ApJ*, 682, 1041
- Rybicki, G. B., & Lightman, A. P. 1979, "Radiative processes in astrophysics." (Wiley-Interscience: New York)
- Sazonov, V. N. 1969, *Soviet Astronomy*, 13, 396
- Serabyn, E., Carlstrom, J., Lay, O., Lis, D. C., Hunter, T. R., Lacy, J. H. 1997, *ApJ*, 490, L77
- Shafee R., McKinney J. C., Narayan R., Tchekhovskoy A., Gammie C. F., McClintock J. E., 2008, *ApJ*, 687, L25
- Sharma, P., Quataert, E., Hammett, G. W., & Stone, J. M. 2007, *ApJ*, 667, 714
- Sharma, P., Quataert, E., Stone, J. M. 2008, *MNRAS*, 389, 1815
- Shcherbakov, R. V. 2008, *ApJ*, 688, 695
- Shcherbakov, R. V., Baganoff F. K. 2010, *ApJ*, 716, 504
- Shcherbakov, R. V., Huang, L. 2010, *MNRAS*, 410, 1052
- Shen, Z.-Q., Lo, K. Y., Liang, M.-C., Ho, P. T. P., Zhao, J.-H. 2005, *Nature*, 438, 62
- Shkarofsky, I. P., Johnston, T. W., Bachynski, M. P. 1966, "The particle kinetics of plasma," (Addison-Wesley Publishing Company: London)
- Tchekhovskoy, A., McKinney, J. C., Narayan, R. 2007, *MNRAS*, 379, 469
- Yuan, F., Markoff, S., & Falcke, H. 2002, *A&A*, 383, 854
- Yuan, F., Quataert, E., Narayan, R. 2004, *ApJ*, 606, 894
- Yusef-Zadeh, F., Wardle, M., Cotton, W. D., Heinke, C. O., Roberts, D. A. 2007, *ApJ*, 668, 47

**Table 2**  
Values of  $\chi_H^2/\text{dof}$  for radiative transfer tests over best models.

Test	spin $a_* = 0$	spin $a_* = 0.5$	spin $a_* = 0.7$	spin $a_* = 0.9$	spin $a_* = 0.98$
$P_N : 75 \rightarrow 111$	0.00467	0.00324	0.00191	0.00460	0.00533
$P_N : 111 \rightarrow 161$	0.00062	0.00103	0.00045	0.00140	0.00018
$P_{ss} : 1.003r_H \rightarrow 1.01r_H$	0.00036	0.00048	0.00095	0.00082	0.00049
$P_{ss} : 1.01r_H \rightarrow 1.03r_H$	0.00891	0.01467	0.01320	0.01332	0.00951
$P_{\text{fact}} : 0.8 \rightarrow 1.0$	0.00896	0.05324	0.13630	0.03617	0.02735
$P_{\text{fact}} : 1.0 \rightarrow 1.2$	0.00171	0.04631	0.12574	0.02501	0.02665
$P_{\text{rhopo}} : Q \rightarrow Q+ = 0.2$	0.03928	0.03743	0.06235	0.02499	0.12360
$P_{\text{Upo}} : Q \rightarrow Q- = 0.1$	0.01305	0.01975	0.02699	0.02118	0.04049
$P_{\text{Bpo}} : -1.0 \rightarrow -0.8$	0.16734	0.31580	0.24751	0.07161	0.18264

Yusef-Zadeh, F., Wardle, M., Heinke, C., Dowell, C. D., Roberts, D., Baganoff, F. K., Cotton, W. 2008, ApJ, 682, 361  
Yusef-Zadeh, F., et al. 2009, ApJ, 706, 348

Zhao, J.-H., Young, K. H., Herrnstein, R. M., Ho, P. T. P., Tsutsumi, T., Lo, K. Y., Goss, W. M., Bower, G. C. 2003, ApJ, 586, 29

## APPENDIX

### RADIATIVE TRANSFER CONVERGENCE

We have created a novel code for GR polarized radiative transfer. As with any new code, we need to conduct a set of convergence tests to ensure it is working accurately. First, we need to devise metrics for assessing accuracy. In the present paper we model fluxes at 7 frequencies between 88 GHz and 857 GHz, LP fractions at 3 frequencies and CP fractions at 2 frequencies and define  $\chi^2$  as to characterize the goodness of fit. We employ a similar quantity  $\chi_H^2/\text{dof}$  to characterize the accuracy of transfer. We define

$$\chi_H^2/\text{dof} = \frac{1}{9} \sum_{i=1}^{12} \frac{(Q_{i,1} - Q_{i,2})^2}{\sigma(Q)^2}, \quad (\text{A1})$$

where  $Q_{i,1}$  are simulated polarized fluxes for one set of auxiliary radiative transfer parameters and  $Q_{i,2}$  are the fluxes for another set. The errors  $\sigma(Q)$  are the observed errors of the mean, and the index  $i$  runs through all fitted fluxes, LP, and CP fractions. When one of the models fits the data exactly, then  $\chi_H^2/\text{dof}$  coincides with  $\chi^2/\text{dof}$ . Auxiliary radiative transfer parameters include:

1. dimensionless scale,  $P_{\text{fact}}$ , of the size of integration region in the picture plane,
2. distance from the center,  $P_{\text{ss}}$ , measured in horizon radii  $r_H$ , where radiative transfer starts,
3. number of points,  $P_{\text{snxy}} = N$ , along each dimension in picture plane,
4. extension power-law slope of density profile,  $P_{\text{rhopo}}$ ,
5. extension slope of internal energy density profile,  $P_{\text{Upo}}$ ,
6. extension slope of magnetic field profile,  $P_{\text{Bpo}}$ .

Since fluctuations and differences in  $\chi^2/\text{dof}$  between different models reach 1, then values  $\chi_H^2/\text{dof} \lesssim 0.1$  are acceptable, but we in general strive for  $\chi_H^2/\text{dof} < 0.02$ . We set constant  $P_{\text{fact}}$ ,  $P_{\text{ss}}$ ,  $P_{\text{snxy}}$  for all radiative transfer computations, but we cannot check the code accuracy for all models. We check the convergence a posteriori for the best at each spin value. We find values of parameters  $P_{\dots}$  by trial-and-error. The resulting set of auxiliary parameters is  $P_{\text{fact}} = 1$ ,  $P_{\text{ss}} = 1.01r_H$ , and  $P_{\text{snxy}} = 111$ . The values of  $P_{\text{rhopo}}$  and  $P_{\text{Upo}}$  are fixed by extensions to large radii and density in the inner flow. The tests and the values of  $\chi_H^2/\text{dof}$  are in Table 2. The first column describes the test. In particular,  $P_{\text{fact}} : 1 \rightarrow 0.8$  means that we tested the convergence of integration region relative size, the value of  $P_{\text{fact}}$  was changed from 1 to 0.8. We change one parameter at a time. Since the power-law slopes  $P_{\text{rhopo}}$  and  $P_{\text{Upo}}$  can vary from model to model, we change them in such a way that rhopo is increased by 0.2 and Upo is decreased by 0.1. This represents variation of density by a factor of 7 and variation of temperature by a factor of 2.5 at the distance  $r_{\text{out}} = 3 \cdot 10^5 M$ , where extension starts from, leading to minor changes in  $\chi_H^2/\text{dof} < 0.1$  (see Table 2). Density and temperature at  $r_{\text{out}} = 3 \cdot 10^5 M$  are known better than to within a factor of several (Baganoff et al. 2003; Shcherbakov & Baganoff 2010). It is unlikely that unjustified power-law extensions of density and temperature to large radii change the polarized spectrum substantially. We also estimate the influence of magnetic field extension power-law by making it shallower from  $(r/M)^{-1.0}$  to  $(r/M)^{-0.8}$ . The resulting  $\chi_H^2/\text{dof} \approx 0.3$  are large, which means the modifications of  $b$  extensions will change the best fits. The extensions as shallow as  $|b| \propto (r/M)^{-0.5}$  may provide better fits to Faraday rotation measure and should be carefully explored. Various extensions of the fluid velocity lead to practically the same polarized intensities.